Journal of Applied Physics REVIEW pubs.aip.org/aip/jap

Quantitative measurements in scanning thermal microscopy: Theoretical models, calibration technique, and integrated instrument

Cite as: J. Appl. Phys. **138**, 050701 (2025); doi: 10.1063/5.0280896
Submitted: 15 May 2025 · Accepted: 11 July 2025 ·
Published Online: 1 August 2025

Yifan Li,[1,2] Jiang Wu,[1] Jing Luo,[1] Jianli Wang,[3] Wei Yu,[1] and Bingyang Cao[2,a)]

AFFILIATIONS

[1]School of Energy and Materials, Shanghai Polytechnic University, Shanghai, 201209, China
[2]Key Laboratory for Thermal Science and Power Engineering of Ministry of Education, Department of Engineering Mechanics, Tsinghua University, Beijing 100084, China
[3]Jiangsu Key Laboratory for Design and Manufacture of Micro-Nano Biomedical Instruments, Department of Mechanical Engineering, Southeast University, Nanjing 210096, China

Note: This paper is part of the Special Topic on Thermal Transport in Micro/Nanostructured Materials and Devices.
[a)]**Author to whom correspondence should be addressed:** caoby@tsinghua.edu.cn

ABSTRACT

Thermal management at the micro/nanoscale has emerged as a critical bottleneck limiting device performance and reliability. Scanning Thermal Microscopy (SThM), owing to its nanoscale spatial resolution and surface thermal response characterization capabilities, has been extensively employed to probe localized thermal properties. However, achieving quantitative SThM measurements remains challenging due to the complex coupled thermal transport at the probe–sample interface. This review systematically summarizes the advances over the past two decades in enabling quantitative thermal property measurements using SThM, focusing on three primary aspects: theoretical modeling, calibration strategies, and instrument integration. Theoretical developments have addressed multipath thermal transport mechanisms, with analyses of each model's applicability under distinct heat transport regimes. Calibration approaches covered the implicit and explicit thermal exchange calibrations, as well as double-scan and Null-point techniques for thermal conductivity and temperature field alignment. Instrument integration encompasses advanced configurations such as 3ω-SThM, MEMS-based thermal platforms, and thermal probe optimization, along with the mechanisms by which they enhance measurement sensitivity and spatial resolution. Despite substantial progress, the quantitative implementation still encounters challenges related to the limited integration of theoretical thermal transport models into practical calibration protocols. One of the primary reasons lies in the inherent complexity and limited accuracy of modeling the coupled thermal transport at the probe–sample interface. Future advancements may leverage data-driven machine learning methods and multimodal strategies (such as integrated pump–probe methodologies) to further expand the applicability and improve the quantitative precision of SThM-based thermal characterization.

I. INTRODUCTION

With the continued miniaturization, heterogeneous integration, and increasing power density of electronic devices, thermal management has become a critical bottleneck limiting further improvements in device performance and reliability. Accurate measurement and understanding of thermal properties (such as thermal conductivity and thermal resistance) within device structures are essential for optimizing thermal design and management strategies. At the nanoscale, heat transport behavior can significantly deviate from classical Fourier's law due to effects such as phonon-interface scattering, boundary limitations, and quantum phenomena.[1] Moreover, emerging materials (such as graphene, MoS_2, black phosphorus, and MXenes) exhibit strong anisotropy and interlayer coupling effects, which are often obscured by conventional macroscale measurements. Therefore, the development of high-resolution and high-sensitivity

thermal characterization techniques at the nanoscale is vital for elucidating intrinsic heat transport mechanisms and uncovering the structure–property relationships that govern thermal performance.

Micro-nanoscale thermal characterization techniques can be broadly categorized into non-contact and contact-based methods. The former primarily involves optical approaches, including infrared thermography,[2] thermoreflectance imaging,[3] Raman thermometry,[4] and thermoreflectance techniques.[5] Contact-based methods are generally electrical, such as direct thermocouple-based techniques,[6] micro-resistance thermometry,[7] and scanning thermal microscopy (SThM), which relies on thermoelectric signal conversion.[8] Non-contact methods offer advantages such as non-invasiveness and strong compatibility with various materials. However, their testing results are strongly dependent on material-specific optical or thermal models. Contact-based methods typically exhibit higher local sensitivity, making them well-suited for studying nanoscale heat transport phenomena. Built on the SPM platform, the tip-based contact measurement of SThM allows direct spatial mapping of thermal property or temperature with sub-100 nm spatial resolution. It enables simultaneous topography-thermal imaging, which is particularly useful for heterogeneous and anisotropic materials, such as nanocomposites, 2D materials, and nanostructured devices. These advantages make SThM a powerful tool for localized thermal analysis across various advanced material systems.

The fundamental principle of SThM lies in the integration of a thermosensitive element at the probe tip, which senses local variations in thermal conductivity or temperature by contacting or approaching the sample surface in the near field.[9] By scanning across the sample surface, a spatial map of heat transfer between the probe and sample can be obtained. When local thermal equilibrium is achieved between the probe tip and the sample, a spatial temperature distribution of the surface can be reconstructed. Furthermore, if the heat flux is known or controlled, the local thermal properties of the sample can be quantitatively extracted.[10] The spatial resolution of SThM primarily depends on the probe design and operating environment. Under ambient conditions, water meniscus effects and surface adsorbates typically limit resolution to ∼50 nm; however, in vacuum environments, where such effects are minimized, resolutions below 10 nm have been reported using optimized probe designs.[11,12] As a contact-based technique, the heat flow required to maintain the tip at a constant temperature is directly influenced by the thermal properties of the sample and can also be affected by the surface topography. However, due to the complex and coupled heat transfer mechanisms at the tip–sample contact interface,[13] it remains difficult to accurately estimate the interfacial thermal resistance. Consequently, the lack of a well-defined correlation between the measured signals and intrinsic thermal parameters poses a significant challenge to achieving quantitative nanoscale thermal property characterization.

Since SThM was first introduced by Williams and Wickramasinghe in 1986,[14] several review articles have been published. Early contributions by Gmelin *et al.* and Majumdar toward the end of the last century summarized the basic working principles and representative applications of the instrument.[15] About a decade ago, Wielgoszewski and Gotszalk provided a detailed overview of nanoscale temperature and thermal property mapping,[16] while around the same period, Gomès *et al.* devoted considerable attention to reviewing the operational mechanisms of various types of thermal probes.[10] More recently, comprehensive review articles published in the past five years have provided broader coverage of the development history, underlying principles, and practical applications,[17] offering valuable insight for researchers newly entering the field. However, concerning the core challenge in SThM application- quantitative thermal measurements, only Bodzenta *et al.* have systematically addressed this issue in their 2020 tutorial and 2022 perspective articles.[18,19] These works focused on temperature and thermal conductivity measurements, providing a foundational summary of quantitative approaches. This review presented here aims to provide a systematic overview of the progress in quantitative measurement over the past two decades. Specifically, it highlights advances and key breakthroughs in three main areas that have driven the quantitative evolution of SThM: theoretical modeling, calibration strategy, and integrated instrument. Distinct from previous reviews, this work aims to provide a structured and application-oriented perspective, offering a clear roadmap for improving the measurement accuracy and practical applicability of SThM in nanoscale thermal analysis.

II. THEORETICAL MODELING

Quantitative thermal measurements using SThM rely not only on sensitive instrumentation but also on the ability to relate the measured electrical signals to physical thermal properties. This requires rigorous thermal modeling to describe heat transfer across the tip–sample interface and surrounding structures. Analytical and numerical models enable the inverse extraction of parameters such as local thermal conductivity, interfacial resistance, and heat capacity, by interpreting the spatial and frequency-dependent response of the probe. As such, theoretical modeling serves as a critical link between raw measurements and physically meaningful data and, thus, is a fundamental component of quantitative SThM analysis.

This probe–sample interface typically involves multiple heat transfer channels: mechanical contact, conduction through air or water meniscus, and thermal radiation. Neglecting or misinterpreting the contribution of any of these pathways can lead to significant errors in evaluating the local thermal properties of the sample. Therefore, accurate modeling and analysis of interfacial thermal resistance and heat flux pathways form the foundation for reliable quantitative thermal characterization.

A. Basic heat transfer mechanisms

Considering the coupling of multiple interfacial heat transfer mechanisms that existed in the probe–sample contact area, Fig. 1, it is accepted that the total thermal resistance between the probe and sample can be expressed by the following parallel model, Eqs. (1) and (2):[20]

Contact mode,

$$\frac{1}{R_{interfacial}} = \frac{1}{R_{air}} + \frac{1}{R_{water}} + \frac{1}{R_{rad}} + \frac{1}{R_{mc}}. \tag{1}$$

Non-contact mode,

$$\frac{1}{R_{interfacial}} = \frac{1}{R_{air}} + \frac{1}{R_{rad}}. \tag{2}$$

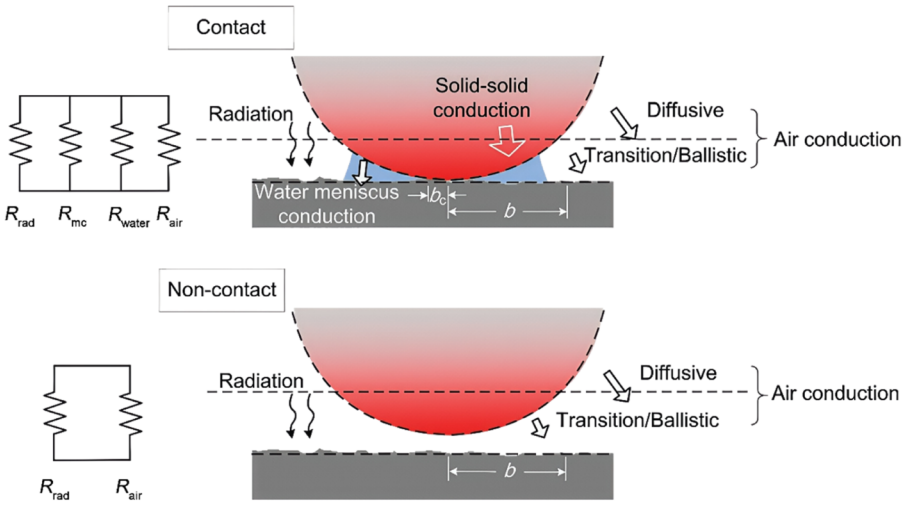

FIG. 1. Schematic multiple interfacial heat transfer mechanisms exist in the probe–sample contact area under contact and non-contact mode [Reprinted with permission from Zhang *et al.*, Adv. Funct. Mater. **30**(18), 1900892 (2020). Copyright 2019, Wiley-VCH Verlag GmbH & Co. KGaA.].

Here, $R_{interfacial}$ is the total interfacial thermal resistance, R_{air} is the thermal resistance caused by the air gap, R_{water} is the thermal resistance caused by the water meniscus, R_{rad} is the thermal radiation-based resistance, and R_{mc} is the mechanical contact resistance. In contact mode, thermal conduction across the probe–sample interface dominates, making it suitable for quantitative thermal conductivity measurements. In non-contact mode, heat transfer occurs primarily via near-field radiation or gas conduction, enabling imaging of soft or delicate surfaces without mechanical interference, though with reduced spatial resolution and more complex calibration.

It should be noted that SThM typically operates in the contact mode, but in such cases, the actual contact area between the probe and the sample may still be relatively small. The heat transfer may also occur via adjacent non-contact regions, including air conduction, near-field radiation, and water meniscus. Therefore, Eq. (1) is intended to conceptually represent the various parallel heat flow channels, rather than serve as an exact analytical solution. The air heat transfer channel, though limited in well-established contact, may still be relevant due to surface roughness and nanoscale separation zones. Sections II B–II E provide a detailed overview of the influencing factors and calculation methods associated with each heat transfer mechanism.

B. Water meniscus conduction

The water meniscus exists when the test is performed in atmospheric conditions. A typical model for calculating the thermal conductivity of the water meniscus is based on the contact geometry. Assy *et al.* investigated the role of the water meniscus in the interfacial area, indicating that the water meniscus gradually evaporates with the increased probe temperature, leading to a significant reduction in its contribution to heat conduction.[21] They estimated the thermal conductance of the water meniscus (G_{water}) using Eq. (3) by analyzing the relationship between pull-off forces and temperature,

$$G_{water} = 2\pi k_w S_w. \tag{3}$$

Here, k_w is the water thermal conductivity and S_w is the shape factor related to the tip–sample separation, meniscus width, and the angle of the apex. Their group and Shi *et al.* suggested that, under certain experimental conditions, the G_{water} contributes less significantly to the total probe–sample heat interaction compared to mechanical contact. However, it is important to note that G_{water} can become dominant under high humidity or low contact pressure, and its influence strongly depends on environmental conditions and probe heating.[22]

C. Air conduction

R_{air} should be considered if the testing was not performed in the vacuum. Fourier's law can be used to describe the heat conduction by the air gap since the heat transfer distance is larger than the mean free path (MFP) of the air (~65 nm at 300 K, 1 atm),[23] Eq. (4),

$$R_{air} = \frac{d_{air}}{k_{air} \cdot A}. \tag{4}$$

Here d_{air} is the thickness of the air gap, k_{air} is the thermal conductivity of the air, and A is the contact area related to the tip geometry and heat area. When the test was performed in the contact mode, the heat transfer distance was much smaller than the MFP of the air, the continuum assumption for heat conduction broke down, and Fourier's law was no longer valid. Instead, heat transfer through the air gap enters the ballistic or quasi-ballistic regime. Several excellent reviews on non-Fourier heat conduction are already available in the literature,[1,24,25] and the detailed discussion will not be repeated here. Table I summarizes the three methods that are representative of calculating the effective thermal conductivity of air considering non-Fourier heat conduction, including Direct Simulation Monte Carlo (DSMC), Ballistic-Diffusive model (BDM), and Smoluchowski model. Based on statistical simulation, DSMC is suitable for fundamental studies involving free-molecular or transition regimes, offering high accuracy in modeling molecular interactions. However, it is computationally intensive.

TABLE I. The representative methods for effective thermal conductivity of air calculation considering non-Fourier heat conduction (k_{eff} is the effective thermal conductivity considering the non-Fourier heat conduction).

Method	Expression	Principle
DSMC[26]	$k_{eff} = \frac{q}{\nabla T}$, $q = \frac{1}{V}\sum_i \frac{1}{2} m_i v_{i,x}(v_i^2)$	Accurate and direct simulation of molecular transport and heat transfer, suitable for detailed modeling of heat transport
BDM[27]	$k_{eff} = \frac{q}{\nabla T}$, $q = q_{diff} + q_{ballistic}$	Considering the diffusion-ballistic coupling and requiring careful adaptation since the original framework was developed for phonon transport in solids
Smoluchowski model[28]	$k_{eff} = \frac{k_{air}}{1 + \frac{2\beta\lambda}{d_{air}}}$	Considering the ratio between the MFP of air (λ) and the gap thickness (d_{air}), corrected by a slip-flow model

BDM is a semi-analytical approach capturing both ballistic and diffusive transport. Originally formulated for phonons in solids, it can be adapted to describe gas conduction but may require modification for specific media. The Smoluchowski model focuses on the reduction of thermal conductivity due to slip-boundary effects in narrow gaps. It offers a simple correction for gas conduction but is empirical and less accurate in highly rarefied conditions.

D. Thermal radiation

The calculation of thermal radiation at the probe–sample interface strongly depends on their separation distance. When the separation distance is much greater than the Wien wavelength (~10 μm), classical Planck's law can be used to describe thermal radiation, Eq. (5). However, when the separation distance is smaller than the Wien wavelength (especially below 100 nm), evanescent waves can tunnel across the gap,[29] significantly enhancing radiation beyond the blackbody limit. Under such near-field conditions, Planck's law is no longer applicable. At such distances, the near-field photon tunneling significantly enhances radiative heat transfer, making it a dominant channel for thermal exchange at the nanoscale. Modeling near-field radiative heat transfer (NFRHT) typically relies on fluctuational electrodynamics (FE) based on Rytov's theory, and several numerical approaches including finite-difference time-domain (FDTD) simulations, thermal discrete dipole approximation (TDDA), volume integral equation (VIE) methods, and surface integral equation (SIE) methods. The details of these models can be found in some excellent reviews,[30,31] while the core expression and principles are briefly summarized here in Table II. Given the extremely small air gap and the complex geometry of thermal probes, fluctuational electrodynamics is the most widely adopted theoretical approach, while TDDA and SIE are

TABLE II. The representative models for evaluating NFRHT.

Models	Expression	Principle
FE[32]	$P = \int_0^\infty \frac{d\omega}{2\pi}[\Theta(\omega \cdot T_1) - \Theta(\omega \cdot T_2)]T(\omega)$	Introducing temperature information by thermally fluctuating current source terms
FDTD[33]	$E^{n+1} = E^n + \frac{\Delta t}{\varepsilon}\left(\nabla \times H^n - J^n_{fluc}\right)$, $H^{n+1} = H^n - \frac{\Delta t}{\mu}\left(\nabla \times E^{n+1}\right)$	Discretizing Maxwell's equations into an FD format, and simulating the propagation of electromagnetic fields through time-stepping in the time domain
TDDA[34]	$p_i = \alpha_i\left(E_{inc,i} + \sum_{j\neq i} G_{ij}p_j\right)$, $\Phi(\omega) = \frac{2}{\pi}\omega \mathrm{Im}\left[\sum_{i,j} p_i^\dagger \cdot \mathrm{Im}[G_{ij}] \cdot p_j\right]$	Discretizing the object into a network of dipoles, thermal radiation is calculated based on the interactions
VIE[35]	$E(r) = E_{inc}(r) + \int_V G(r, r') \cdot \chi(r') \cdot E(r')\mathrm{d}r'$	Calculating the electric field response by treating the electric polarization within the object volume as the integral source
SIE[36]	$E(r) = E_{inc}(r) + \int_S [J(r') \times \nabla' G(r, r')]\mathrm{d}S'$	Calculating the contributions of surface electric and magnetic currents to the external field

commonly employed numerical methods due to their adaptability to complex geometries and material configurations,

$$I(\nu,T) = \frac{2h\nu^3}{c^2} \cdot \frac{1}{\exp\left(\frac{h\nu}{k_B T}\right) - 1}. \quad (5)$$

Here, I is the blackbody radiation intensity within a unit frequency range, h is the Planck constant, ν is the frequency, and K_B is the Boltzmann constant. In modeling NFRHT between the SThM probe and the sample, FE serves as the fundamental theoretical framework, providing qualitative insight and guiding model development. TDDA offers the most practical balance between accuracy and computational efficiency, making it well-suited for simulating localized thermal radiation from sharp probe geometries. For more complex geometries or dynamic behaviors (such as probe scanning or modulated heating), FDTD methods offer enhanced simulation capabilities. Although VIE and SIE methods are theoretically rigorous, their applicability in SThM is limited due to geometric constraints and incompatibility with sharp features. They are mainly used for validation and supplementary analysis under simplified or regular geometries.

It is worth noting that although near-field thermal radiation may theoretically play a significant role in probe–sample heat transfer in SThM operated under vacuum conditions, most existing modeling efforts have not systematically incorporated this mechanism. This omission is primarily due to the high computational complexity, challenges in experimental validation, the absence of standardized modeling frameworks, and the prevailing dominance of solid-state conduction in current experimental settings.

E. Mechanical contact conduction

R_{mc} existed when the test was performed in contact mode. Strictly speaking, R_{mc} comprises both microscopic thermal boundary resistance ($R_{boundary}$, also known as Kapitza thermal resistance) arising from the mismatch of heat carriers across the solid–solid interface and macroscopic contact resistance ($R_{contact}$).[37] Typical methods for calculating $R_{boundary}$ include the Newtonian mechanics-based lattice dynamics (LD) and molecular dynamics (MD); Green's function (GF) approaches, which characterize the system's response to perturbations; and the Boltzmann Transport Equation (BTE), which describes the distribution and transport of thermal carriers. Detailed discussions of these methods can be found in existing reviews,[38,39] while their core expressions and key characteristics are summarized in Table III. The typical $R_{boundary}$ value falls between 10^{-9} and 10^{-8} m^2 K/W for the electron–electron coupling interface (for the thermal carriers of the sample are electrons) and $10^{-7} \sim 10^{-6}$ m^2 K/W for the electron–phonon interface (for the thermal carriers of the samples are phonons).[40] MD is the most suitable method for characterizing the intrinsic thermal resistance at the contact interface between the probe and sample surface. It accurately captures nonlinear and non-equilibrium heat transport at the atomic scale, even under non-ideal conditions such as rough, amorphous, or heterogeneous interfaces commonly encountered in practical contacts.

Although analytical models for $R_{boundary}$ are not directly applicable to all SThM systems due to the lack of full phonon spectra and idealized assumptions, they provide valuable theoretical foundations for understanding phonon transmission across solid–solid interfaces. The inclusion of these models in this review is intended not for plug-in numerical calculation, but to highlight the physical origins, assumptions, and predictive differences between microscopic interfacial thermal resistance models. They help contextualize the challenges in quantifying nanoscale thermal contact in SThM, particularly in contrast to the limited theoretical treatment available for macroscopic contact resistance at the probe–sample interface.

It is worth noting that mechanical contact interfaces are inherently non-ideal. Due to the effects of surface roughness, contact pressure, and the mechanical properties of the materials involved, real contact typically occurs at a discrete set of microscopic asperities, through which the majority of heat is transferred. When the surface

TABLE III. Typical methods for calculating $R_{boundary}$ (represented by R_b in the table).

Type	Model	Characteristic
LD[41]	$R_b = \frac{1}{\int_0^\infty \hbar\omega\Gamma_{LD}(\omega)\frac{\partial\bar{n}(\omega,T)}{\partial T}d\omega}$	The exact lattice structure required
MD	NEMD:[42] $R_b = \frac{\Delta T}{J}$, $J = \frac{1}{2tA}\sum_{transfer}\frac{m}{2}\left(v_{hot}^2 - v_{cold}^2\right)$	The proper potential function required
	EMD (infinitely large system):[43] $R_b = \frac{k_B T^2}{A\int_0^\infty \langle J(t)J(0)\rangle \mathrm{d}t}$	
	EMD (finite system):[43] $R_b = \frac{e^{-wt_s}k_B T^2}{A\int_0^{t_s}\langle J(t)J(0)\rangle \mathrm{d}t}$	
GF[44]	$R_b = \frac{2\pi A}{\int_0^\infty \hbar\omega\frac{\partial\bar{n}(\omega,T)}{\partial T}\Xi(\omega)\mathrm{d}\omega}$.	Exact lattice structure and force constants required
BTE[45]	$R_b = \frac{4}{\int_0^{\omega_{max}}\hbar\omega\sum_p\left(v(\omega,p)\mathrm{D}(\omega,p)\right)\frac{\partial\bar{n}(\omega)}{\partial T}\Xi(\omega)\mathrm{d}\omega}$.	Empirical boundary condition

roughness is significant, non-contact regions may contribute to interfacial heat transfer via conduction through the air gap or water meniscus formed by capillary condensation. These contributions are highly sensitive to surface roughness and have been identified as sources of topography-induced artifacts in many studies.[21,46] In contrast, when the sample surface is sufficiently smooth (with roughness below a few nanometers), the thermal resistance at the interface becomes less dependent on contact quality, and heat conduction through mechanical contact tends to stabilize. Zhang *et al.* reported that typical thermal resistance values fall within the range of 0.1–10 $\mathrm{K}\,\mu\mathrm{W}^{-1}$.[17] Considering that the thermal contact area at the probe tip is typically on the order of $10^{-12}\,\mathrm{m}^2$, the corresponding $R_{contact}$ is estimated to be in the range of 10^{-7}–$10^{-5}\,\mathrm{m}^2\,\mathrm{K/W}$. The comparison with $R_{boundary}$ values reveals that, for samples where electrons are the dominant heat carriers, $R_{contact}$ is typically sufficient to describe the R_{mc}. However, for phonon-dominated systems, the contribution of the $R_{boundary}$ cannot be neglected. This understanding provides a fundamental basis for the calibration strategies aimed at various types of testing materials. The difficulty in quantitatively determining the mechanical contact thermal resistance remains one of the major challenges in achieving quantitative SThM measurements, and this issue will be further addressed in Sec. III.

Obtaining quantitative information on the contributions of different heat transport channels would be of high value to the SThM community. However, it is neither feasible nor necessarily meaningful. The dominant heat transfer mechanism at the probe–sample interface varies significantly depending on the measurement mode and environmental conditions. In contact mode, under either ambient or vacuum conditions, mechanical conduction typically serves as the primary heat exchange pathway (especially under tightly pressed contact or when the surface roughness is low). In non-contact mode, air conduction dominates under ambient conditions, and ballistic heat transport may also need to be considered. In contrast, under vacuum conditions, as the probe–sample separation enters the submicrometer or nanometer regime, near-field radiative heat transfer becomes significantly enhanced and can emerge as the dominant mechanism. A qualitative understanding of dominant mechanisms under typical conditions provides a more robust and transferable framework for interpreting thermal signals and guiding calibration strategies. Generally speaking, under typical contact-mode measurements in ambient conditions, solid–solid contact conduction is generally considered the dominant heat transfer mechanism, especially when the applied load ensures mechanical contact between the probe and sample. This is also reflected in most subsequent calibration strategies, where interfacial thermal resistance is primarily attributed to mechanical contact, with limited consideration of alternative transport mechanisms.

III. CALIBRATION STRATEGIES

The core function of calibration strategies in SThM is to convert the electrical response detected by the probe into physically meaningful thermal parameters, such as the thermal conductivity or the surface temperature of the sample. Calibration strategies are necessary because interfacial thermal resistance at the probe–sample contact causes the measured signal to deviate from the sample's actual thermal response, making direct interpretation unreliable without proper correction. The measurement modes of the instrument should be clarified before the calibration process. Conductivity contrast mode (CCM) and temperature contrast mode (TCM) are typical working modes. In CCM, the probe is actively heated via an applied current, and heat flows from the probe to the sample. Due to variations in local thermal conductivity, the capacity for heat dissipation differs across the sample, leading to measurable differences in the temperature rise of the probe. In TCM mode, the probe remains unheated or is minimally heated, functioning as a passive sensor. Following appropriate calibration using reference samples at known temperatures, it can be employed to map local temperature variations across the sample surface.[47]

Based on the testing objectives, the calibration strategies can be broadly categorized into two types: sample thermal property calibration and sample temperature reconstruction. The first strategy aims to correlate the probe's temperature rise or signal response with the sample's thermal properties. This process typically involves the use of well-characterized reference materials and can be implemented via two different approaches: implicit thermal exchange calibration (ITEC), which treats the overall heat exchange resistance between probe and sample as a lumped parameter; and explicit thermal exchange calibration (ETEC), which separately evaluates individual components of the thermal transport model for higher accuracy. The latter one is aimed at obtaining the accurate sample temperature via the correction of the thermal non-equilibrium between the probe and the sample, mainly including the double-scan technique and the null-point method. It should be noted that the temperature sensor calibration procedure should be performed first before the above-mentioned calibration strategies since both of them rely on an accurate relationship between the probe's electrical signal and its actual temperature. Without this fundamental calibration step, subsequent analyses may suffer from significant systematic errors or misinterpretations of thermal transport behavior.

A. Temperature sensor calibration

The principle of temperature sensor calibration is based on the temperature-dependent change in the electrical resistance of metallic materials, which follows either a linear or nonlinear relationship. A quantitative correlation is established between the probe resistance and its actual temperature under a small temperature variation, Eq. (6), enabling electrical measurement and calibration of the probe temperature,

$$R(T) = R_0[1 + \alpha(T - T_0)]. \tag{6}$$

Here, R (T) is the electrical resistance at the temperature T, R_0 is the electrical resistance at room temperature, and α is the temperature coefficient of resistance. This linear approximation is valid typically within a moderate temperature range (e.g., <50 K). For larger temperature variations, a higher-order polynomial fit or empirical calibration is generally required to ensure accuracy.

In earlier studies, there were also reports attempting to extract sample temperature or thermal conductivity information directly from temperature sensor calibration. This strategy typically involves the following steps: establishing the relationship between the probe resistance and its temperature, deriving the overall thermal resistance from the power–temperature rise curve, and isolating the

TABLE IV. ITEC models and corresponding expressions and parameters.

Model	Expression	Parameters
Wilson *et al.*[51]	$R_{interfacial} = \frac{\Delta T \cdot A_{probe}}{T^2 r_0 (1 + \alpha \cdot \Delta T) L}$. (8)	A_{probe}: cross-sectional area of the probe, r_0: electrical resistivity per unit length of the probe, L: probe length
Fleurence *et al.*[52]	$\frac{\Delta R_s}{\Delta R_{SiO_2}} = \frac{a \times k_s}{b + k_s} + c$. (9)	ΔR: probe resistance changes between contact and non-contact mode, a, b, c: parameters obtained by Bayesian inversion fitting
Leitgeb *et al.*[53]	$\Delta V_{layer} = a' + b' \times k_s^{c'}$. (10)	ΔV_{layer}: voltage change at the contact layer, a', b', c': empirical fitting coefficient

thermal resistance component associated with the probe–sample contact.[18] It allows the sample surface temperature to be back-calculated from the measured electrical response. Mittereder *et al.* achieved accurate measurements of channel temperatures in GaAs PHEMTs and MESFETs using a precisely calibrated thermal resistor probe, observing that the terminal voltage of the thermal probe is linearly positively correlated with the temperature of the GaAs transistor.[48] Their results demonstrated excellent agreement with the values estimated using the Cooke thermal model,[49] which is commonly employed to calculate transistor channel temperature. Meinders performed quantitative thermal conductivity measurements of nanoscale thin films using a resistive temperature sensor probe based on a temperature rise approach.[50] They monitored the change in probe resistance before and after contacting the sample to determine the temperature rise. The equivalent thermal resistance formed between the probe and the sample is described by Eq. (7). The heat flow was calculated from the electrical power generated by a constant applied current. The thermal conductivity of the sample (k_s) was then extracted using a thermal constriction resistance model ($R_s = 1/4k_s r$, R_s is the sample thermal resistance and r is the effective contact radius). It represents a typical application of resistive-type thermal probes for steady-state, quantitative thermal analysis,

$$\frac{d(T_{tip} - T_\infty)}{dQ_S} = R_{tip} + R_s. \tag{7}$$

Here, $T_{tip} - T_\infty$ is the total temperature decay and Q_s is the sample heat flow. It is worth noting that the steady state was considered in the above-mentioned cases, the correlation between probe temperature and the thermal response from the sample was established without accounting for interfacial thermal resistance, which introduces certain limitations to the accuracy of the extracted information.

B. ITEC

ITEC is a calibration method that does not require specific thermal exchange parameters. Its fundamental principle involves measuring the thermal response of the probe on a reference sample with well-characterized thermal behavior, thereby establishing a relative relationship between the probe response and thermal conductivity. This relationship is then applied to the comparative analysis of unknown samples. The typical procedure includes: selecting and measuring the thermal signal of a standard reference sample, measuring the target sample under identical testing conditions, and normalizing or differencing the target signal concerning the reference signal to obtain qualitative or semi-quantitative information on local thermal conductivity or heat flux variations. This approach simplifies the complex modeling and thermal resistance measurements required in conventional calibration methods and improves experimental efficiency.

Table IV summarizes ITEC models and corresponding expressions and parameters. Wilson proposed a probe–sample thermal exchange model considering the contact geometry and interfacial heat transfer, illustrated in Fig. 2(a).[51] The experimental data were fitted by adjusting the proposed model parameters, including thermal exchange radius and contact thermal resistance, Eq. (8). Three calibration strategies (the implicit method, the stepwise method, and the intersection method) were compared, and the intersection method was demonstrated to offer higher accuracy in thin-film thermal conductivity measurements. Fleurence *et al.* established an empirical calibration model based on bulk materials with known thermal conductivities.[52] Using a Bayesian statistical inversion approach, they simultaneously estimated both the calibration parameters and the sample's property, Eq. (9), providing a robust framework for uncertainty quantification. The entire workflow of the quantitative SThM measurements is shown in Fig. 2(b). Leitgeb *et al.* established a functional relationship between the probe output voltage and thermal conductivity using an implicit fitting method based on reference thermal conductivity values obtained from TDTR measurements, Eq. (10).[53] This approach enabled quantitative thermal conductivity mapping and represents a typical application of the implicit thermal conductivity calibration strategy for high-resolution thermal image reconstruction under vacuum conditions. Zheng *et al.* achieved quantitative thermal conductivity measurements of perovskite thin films using SThM combined with a semi-empirical model.[54] By fitting empirical constants on reference materials with known thermal conductivity, they established an implicit relationship between the thermal conductivity and the electrical signal.

It is worth noting that the ITEC method has been gradually replaced in recent studies by ETEC strategies. This shift is primarily due to the limitations of ITEC, which relies heavily on empirical fitting, offers limited generalizability and physical transparency, and lacks traceable error sources. As a result, ITEC falls short of meeting the accuracy requirements of high-precision quantitative thermal measurements.

C. ETEC

ETEC is a calibration method based on physical heat transfer models. Its fundamental principle involves incorporating parameters such as the probe–sample contact thermal resistance, the intrinsic thermal resistance of the probe, and the thermal conductivity of the sample into a well-defined thermal conduction model. By performing measurements on a series of standard samples with known thermal

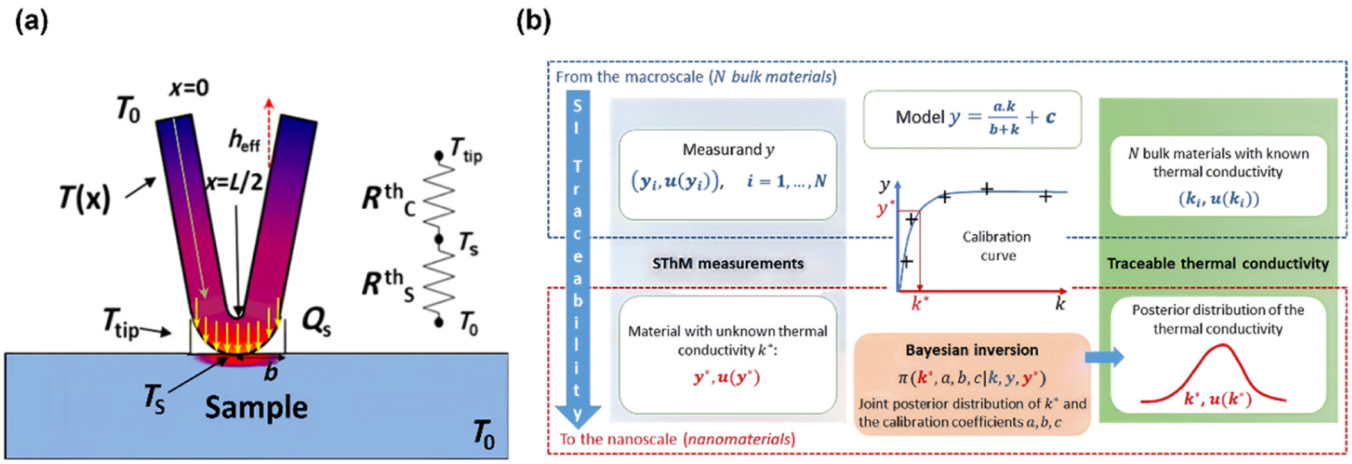

FIG. 2. (a) Probe–sample thermal exchange model proposed by Wilson *et al.* [Reprinted with permission from Wilson *et al.*, MRS Commun. **9**, 650–656 (2019). Copyright 2019, Cambridge University Press]. (b) The schematic of the SThM measurements, Bayesian inversion, and traceable thermal conductivity proposed by Fleurence *et al.* [Reprinted with permission from Fleurence *et al.*, Nanomaterials **13**, 2424 (2023). Copyright 2023, MDPI].

conductivities, the unknown parameters in the model can be fitted, thereby establishing a quantitative relationship between the thermal response signal and the actual thermal conductivity. The typical procedure includes: constructing a thermal model that explicitly defines the heat exchange pathways and parameters, selecting multiple standard samples with known thermal conductivities for measurement, fitting the model to extract system parameters (e.g., contact thermal resistance), and applying the calibrated model to quantitatively determine the thermal conductivity of unknown samples.

Table V summarizes representative analytical models adopted in various implementations of the ETEC. Although these models originate from studies involving different probe geometries, material systems, and sample configurations, they all aim to extract thermal conductivity or thermal conductance by explicitly modeling individual thermal resistances in the probe–sample system. This comparative format helps to understand how modeling assumptions and sample geometry affect the formulation of ETEC and supports model selection for specific experiments. Figure 3 shows representative ETEC calibration setups and probe structures with the detailed statement shown below, highlighting the diversity of platforms and the adaptability of ETEC strategies.

Fischer developed a heat flux equation considering the contact geometry to characterize the thermal interaction between the probe and the sample, Eq. (11).[55] By fitting the experimental data, relevant parameters were determined, enabling accurate prediction of the thermal conductivity of unknown samples. Wielgoszewski *et al.* proposed a heat flux analysis model based on a thermoelectric analogy, Eq. (12), enabling nonlinear heat flux analysis and allowing for the quantitative determination of the interfacial thermal resistance and boundary thermal conductance between the TSV and the silicon substrate, Fig. 3(a).[56] Ge *et al.* proposed a combined-fin model to describe the thermal spreading resistance at the interface between a rectangular thin film and the thermal probe, Fig. 3(b), incorporating boundary conditions for air convection and substrate heat conduction, Eq. (13).[57] Li *et al.* incorporated fractal theory to describe real contact heat conduction induced by surface geometric irregularities and proposed a combined series-parallel model [Fig. 3(c)] to calculate thermal contact resistance, Eq. (14).[58] The model was validated through both theoretical calculations and experimental measurements. In their other work, they suggested that contact conduction dominates interfacial heat transfer and is strongly influenced by interfacial microscale characteristics.[59] They built a correlation between instrument feedback parameters and sample properties, described by Eq. (15), enabling quantitative measurement of localized thermal conductivity. They further employed this model to verify the size-dependent behavior of thermal conductivity in graphene oxide nanosheets. Zhang *et al.* further developed this model by considering the relationship between temperature and electrical resistance and proposed an optimized model, Eq. (16).[60] Chen *et al.* established a thermal resistance network model based on the heat exchange mechanism between the probe and SiO_2 nanoparticles, Fig. 3(d).[61] The model takes into account the contact resistance (R_c), tip-particle resistance ($R_{t\text{-}p}$), equivalent particle resistance (R_{eq}), particle-substrate resistance ($R_{p\text{-}s}$), and substrate thermal resistance (R_s), enabling accurate determination of the thermal conductivity of individual SiO_2 nanoparticles, Eq. (17). Spièce *et al.* integrated beam exit cross-sectional polishing into the scanning system, Fig. 3(e), creating a wedge-shaped, atomically flat cross section to enable quantitative thermal measurements.[62] By measuring the thermal resistance at different thicknesses, a correlation between the internal thermal spreading resistance (R_s) and the thermal conductivity was established, Eq. (18). They also proposed a thermal conduction model for the resistive probe based on a distributed heater structure, deriving an analytical relationship between the average probe temperature and the heating power, ambient temperature, and multiple thermal resistance pathways, Eq. (19).[63] This relationship enables the extraction of the probe–sample contact thermal resistance from known thermal resistance parameters. Liu *et al.* quantified the relationship between heat flux and thermal conductivity by measuring the resistance difference of the probe in contact and non-contact states and incorporating an analytical thermal model.[64] They developed a

TABLE V. ETEC models and the corresponding expression and parameters.

Model	Expression	Parameters
Fischer[55]	$\frac{\Delta Q}{\Delta T} = \frac{3}{4}\frac{k_p \pi r}{1 + k_p/k_s}$. (11)	k_p: probe thermal conductivity, k_s: sample thermal conductivity, r: contact radius
Wielgoszewski *et al.*[56]	$R_{interfacial} = \frac{T_{tip} - T_0}{Q_{tip-sample}}$. (12)	T_0: sample surface temperature, $Q_{\text{tip-sample}}$: actual heat flux from tip to sample
Ge *et al.*[57]	$R_s = \frac{1}{2\pi k_s \delta}\left[\ln\left(\frac{4\delta}{r}\right) + \frac{L}{\delta}\right]$. (13)	δ: diffusion depth, r: contact radius, L: feature size of the sample
Li *et al.*[58]	$R_{interfacial} = \frac{1}{k_s L^D \left(\frac{2-D}{D}\cdot\frac{A_r}{A_a}\right)^{D/2}}$. (14)	D: Fractal dimension, A_r: real contact area, Aa: apparent contact area
Li *et al.*[59]	$R_{interfacial} = \frac{1}{4k_s r_0} + \frac{H}{\pi k_s F \sigma m}$.(15)	r: contact radius, H: hardness, F: loading force, σ: roughness, m: contact slope
Zhang *et al.*[60]	$U = \frac{R_p^0 (T_p - T_0)(1 + \alpha(T_p - T_0))}{\frac{1}{R_{interfacial}} + \frac{1}{R_s} + \frac{1}{R_{cant}}}$. (16)	U: applied voltage, R_p^0: probe electrical resistance at room temperature, R_{cant}: thermal resistance of the cantilever
Chen *et al.*[61]	$k_p = \frac{1}{2\pi r_p \left(R_{eq,SiO_2} - R_c - R_{t-p} - R_{p-s} - R_s\right)}$.(17)	k_p: thermal conductivity of SiO_2 particle, r_p: radius of the particle, R_{eq} : equivalent thermal resistance of the particle
Spièce *et al.*[62]	$R_s(t) = \frac{1}{\pi k_s a} \cdot f(t_{eff}, k_s, r_{int}, r)$. (18)	r: effective contact radius, t_{eff}: effective thickness considering thermal resistance
Spièce *et al.*[63]	$Q_h = \frac{T_B - T_M}{R_{BA}} - \frac{T_M - T_B}{R_B} - \frac{T_{air}}{R_{air}} + \frac{T_t - T_s}{R_{interfacial}}$. (19)	T_t: tip temperature, T_M: probe temperature, R_{BA}: thermal resistance between the base and the air, R_B: thermal resistance between the probe and the base,
Liu *et al.*[64]	$\frac{R_{pa} - R_{pc}}{R_{pa} - R_0} = \frac{3GG_s}{4GG_s + 8GG_p + 8G_pG_s}$.(20) $\Delta V_{a-c} \propto \frac{k_s}{K_a k_s + K_b}$.(21)	G: thermal conductance between the sample and the probe, Gs: spreading conductance of the sample, $\Delta V_{a\text{-}c}$: the measured voltage shift, K_a, K_b: fitted constant related to contact geometry
Bodzenta *et al.*[65]	$Z_{NTP} = \frac{1}{1 + j2\pi f R_s C}$. (22)	$Z_{\text{NTP.}}$ average temperature rise of the probe, j: imaginary unit, f: scanning frequency, R_s: sample thermal resistance
Bodzenta *et al.*[66]	$U(d) = U_{bulk} + \frac{U_{sub} - U_{bulk}}{1 + \frac{d}{d_0}}$ (23)	U_{bulk}, U_{sub}: measured voltage of the bulk sample and substrate, d_0 is a parameter related to the thermal conductivity of the sample

heat flux expression based on energy conservation and steady-state heat conduction assumptions. The model accounted for key factors such as interfacial thermal resistance, sample thermal conductivity, and thermal contact radius. They established a quantitative relationship between the probe's temperature rise and the sample thermal properties, Eq. (20). An approximate analytical expression was also derived linking the sample's thermal conductivity to the output voltage of the Wheatstone bridge circuit, Eq. (21).

Another commonly used explicated analysis approach is based on the finite element analysis (FEA) of thermal conduction models. Bodzenta *et al.* developed a 3D steady-state thermal conduction model for the interaction between a resistive probe and the sample.[65] They obtained the temperature distribution at the thermal probe–sample interface through finite element modeling (FEM), as illustrated in Fig. 3(f). They also developed a quadrupole chain model incorporating thermal resistance and capacitance and derived a thermal-electrical model, describing the relationship between the average temperature rise of the probe and heat input, Eq. (22).[66]

Later on, they introduced a specific technique driven by both direct and alternating currents to investigate the static and dynamic resistance variations when the thermal probe contacts the sample and proposed a correction model to extract the intrinsic thermal conductivity of the thin film, Eq. (23).[67] Esfahani *et al.* employed an integrated resistive heating probe combined with FEM to achieve quantitative thermal conductivity mapping of three-phase nanocomposites, the comparison of temperature on the tip–sample junction and the sample underneath the probe was shown in Fig. 3(g).[68] By correlating probe resistance changes with temperature rise responses, and constructing a physical mapping between heat flux and thermal conductivity based on an explicit heat diffusion model, they successfully measured thermal conductivities ranging from 0.66 to 80.8 W/mK in multiphase materials. Zhang *et al.* considered the thermal resistance network at the probe–sample interface, Fig. 3(h), and developed a 3D FEM to simulate the heat transfer between the probe and the sample.[69] This model incorporates detailed thermal transport processes under both diffusive and transitional heat conduction

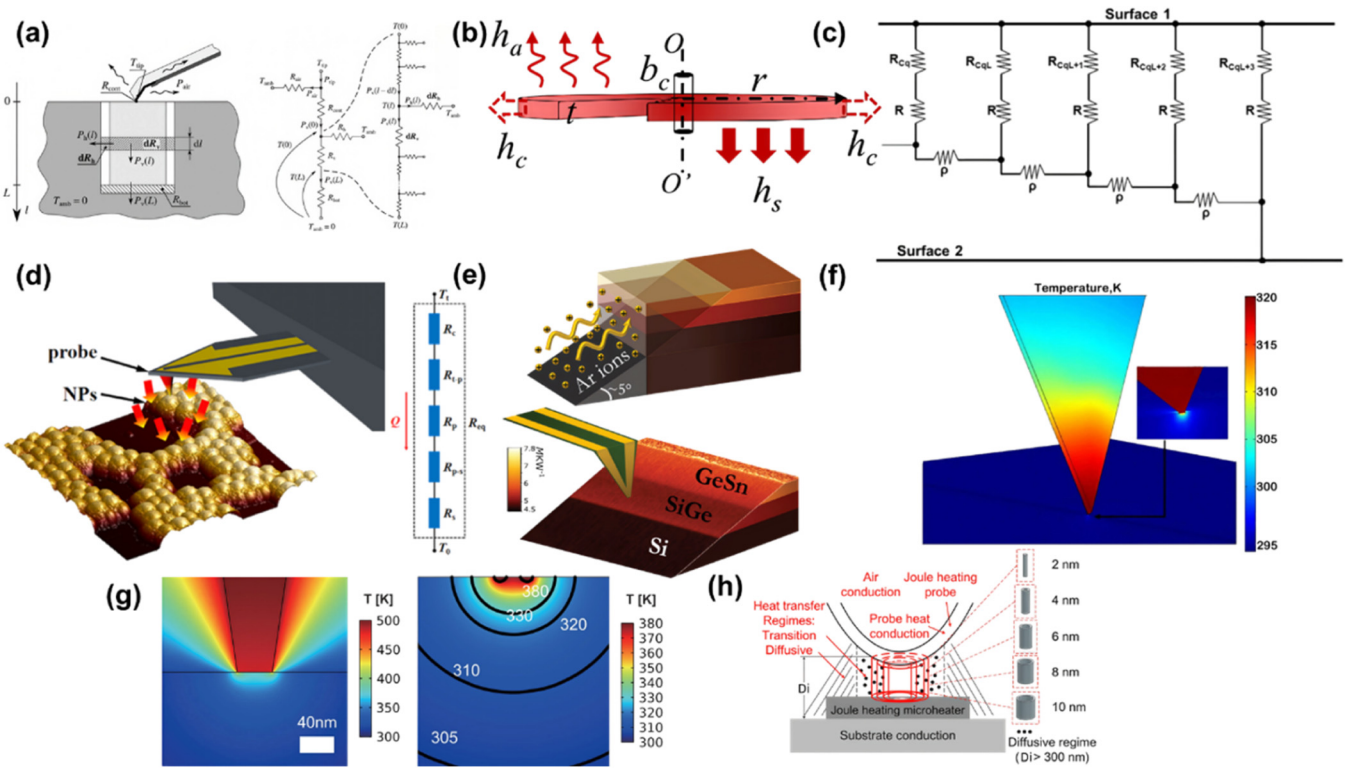

FIG. 3. (a) The heat flux analysis between the probe and TSV together with the equivalent thermal circuit proposed by Wielgoszewski *et al.* [Reprinted with permission from Wielgoszewski *et al.*, Micron **66**, 63–68 (2014). Copyright 2014, Elsevier]. (b) The combined-fin model describing the thermal spreading resistance proposed by Ge *et al.* [Reprinted with permission from Ge *et al.*, Nanotechnology **28**(48), 485706 (2017). Copyright 2017, IOP Publishing]. (c) The fractal theory considering the combination of series and parallel model proposed by Li *et al.* [Reprinted with permission from Li *et al.*, Numer. Heat Transfer, Part A **86**(4), 891–904 (2025). Copyright 2025, Taylor & Francis].[58] (d) The thermal resistance network model between the probe and SiO_2 nanoparticles proposed by Chen *et al.* [Reprinted with permission from Chen *et al.*, Int. J. Heat Mass Transfer **154**, 119750 (2020). Copyright 2020, Elsevier]. (e) Schematic of the beam exit cross-sectional polishing and corresponding SThM measurement proposed by Spièce *et al.* [Reprinted with permission from Spièce *et al.*, Nanoscale **13**, 10829–10836 (2021). Copyright 2021, Royal Society of Chemistry]. (f) FEA analysis of the temperature at the probe–sample contact area proposed by Jerzy *et al.* [Reprinted with permission from Jerzy *et al.*, Int. J. Thermophys. **31**, 150–162 (2010). Copyright 2010, Springer]. (g) Comparison of temperature on the tip–sample junction and the sample underneath the probe by Esfahani *et al.* [Reprinted with permission from Esfahani *et al.*, Natl. Sci. Rev. **5**, 59–69 (2018). Copyright 2018, Oxford University]. (h) 3D FEM modeling with the thermal resistance network considered by Zhang *et al.* [Reprinted with permission from Zhang *et al.*, Rev. Sci. Instrum. **91**, 014901 (2020). Copyright 2020, American Institute of Physics.].

regimes, effectively eliminating uncertainties associated with liquid bridges and mechanical contact.

Regarding practical applications of FEM-based investigation, Zhu *et al.* employed FEA to account for the contact thermal resistance and heat conduction between the SThM probe and the sample, to investigate the influence of secondary phases on the local thermal transport in BiCuSeO-based thermoelectric nanostructures.[70] They found that Pb doping effectively reduced the thermal conductivity of BiCuSeO, while the rGO secondary phase slightly increased it. Bosse *et al.* employed the 3D FEM to quantitatively characterize the nanoscale thermal properties of both amorphous and crystalline phases in $Ge_2Sb_2Te_5$ (a-GST and c-GST) phase-change materials.[71] Guen *et al.* confirmed that non-diffusive thermal transport effects became significant when the contact distance was below 10 μm by using FEM.[72] Shan *et al.* proposed a high-fidelity approach that integrates FEM to analyze the interference of Joule heating in electrocaloric effect measurements and extracted the interfacial thermal resistance between the probe and the sample.[73] Frausto-Avila *et al.* achieved quantitative measurement of the interfacial thermal conductance between MoS_2 and a silicate substrate under ambient conditions by fitting FEM to experimental data.[74] Martinek *et al.* designed a delaminated thin-film structure and extracted local thermal conductivity by comparing thermal signals between delaminated and non-delaminated regions, validated through finite element simulations.[75] Klapetek *et al.* developed a GPU-based finite difference method to simulate topographic artifacts in SThM, incorporating a heat transfer model based on the Poisson equation.[76] This approach enabled the removal of measurement artifacts and improved the accuracy of quantitative thermal measurements.

To sum up, ITEC methods typically involve the use of known reference materials, where the measured signal is compared empirically across samples with different thermal conductivities. ETEC methods rely on detailed thermal modeling of the tip–sample heat transfer, often involving numerical fitting or FEM.

D. Double-scan technique

The double-scan technique was first proposed by Kim *et al.*[77] The fundamental principle of typical double-scan calibration is based on the output voltage signal of a thermocouple-type SThM probe, with calibration achieved through two sequential scans: one in non-contact mode and the other in contact mode. In this approach, the thermal probe is scanned over the same sample area under both conditions, enabling the isolation of the thermal contribution from the probe–sample interface.[75] The probe temperatures in the non-contact and contact states are denoted as T_{nc} and T_c, respectively, while the actual surface temperature of the sample (T_s) lies between these two values. The degree of thermal exchange between the probe and the sample can be expressed using the following empirical relationship, Eq. (24):

$$T_s = T_c + \phi\,(T_c + T_{nc}). \tag{24}$$

The empirical factor ϕ accounts for geometric factors, probe–sample coupling efficiency, and material-dependent thermal contact characteristics. It provides a practical route for semi-quantitative temperature mapping and can be extended to relative thermal conductivity contrast when combined with additional modeling or reference materials. Kim *et al.* investigated the temperature distribution of electrically heated gold lines deposited on Pyrex glass.[78] They found that temperature values obtained using the contact mode were approximately 35% lower than the actual temperature. In contrast, the double-scan technique produced temperature distributions that showed excellent agreement with numerical simulations. Choi *et al.* applied the double-scan technique to decouple non-contact heat transfer components, enabling high-resolution and quantitative measurements of local hotspot temperatures in operating graphene-based electronic devices.[79] The measured and calculated topographic, thermal, and electrical potential profiles are shown in Fig. 4(a). They demonstrated that high graphene-substrate interfacial thermal

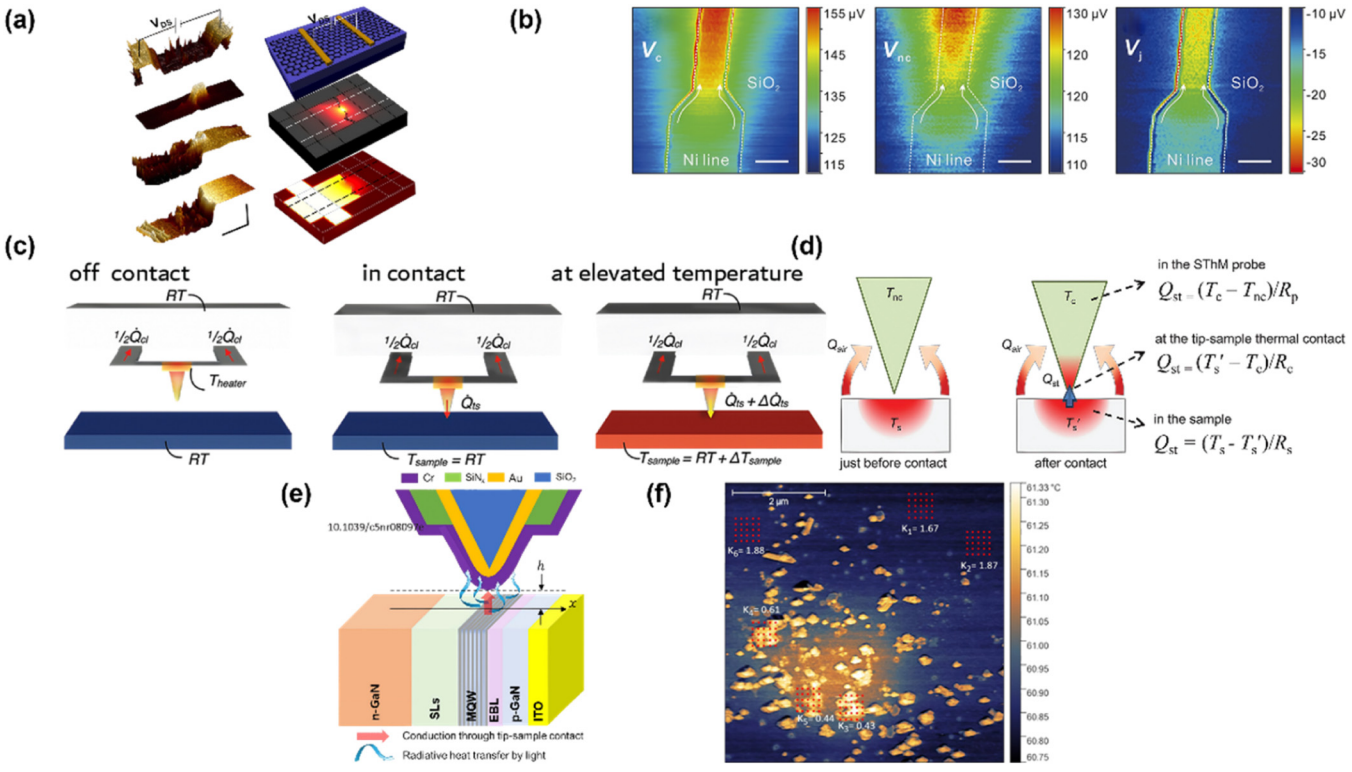

FIG. 4. (a) The measured and calculated topographic, thermal, and electrical potential profiles of graphene-based electronic devices by Choi *et al.* [Reprinted with permission from Choi *et al.*, Appl. Phys. Lett. **110**, 073104 (2017). Copyright 2017, American Institute of Physics]. (b) Comparison of the signal difference under contact and non-contact mode, and the corresponding calibrated results of Ni metal line on a SiO_2/Si substrate by Sun *et al.* [Reprinted with permission from Sun *et al.*, Rev. Sci. Instrum. **93**, 114902 (2022). Copyright 2022, American Institute of Physics]. (c) Schematic of the tip–surface arrangement under different operation state and corresponding thermal resistance change investigated by Menges *et al.* [Reprinted with permission from Menges *et al.*, Nano Lett. **12**, 596–601 (2012). Copyright 2012, American Chemical Society]. (d) Detailed working principle with heat transfer presented of NP-SThM proposed by Ohmyoung Kwon's group [Reprinted with permission from Hwang and Kwon, Nanoscale **8**(9), 5280–5290 (2016). Copyright 2016, Royal Society of Chemistry]. (e) Heat transfer between the thermal probe scanning across the MQW and the cross section of the operating LED investigated by Shin *et al.* [Reprinted with permission from Shin *et al.*, RSC Adv. **13**, 34230–34238 (2023). Copyright 2023, Royal Society of Chemistry]. (f) The thermal image and the thermal conductivity of the local area of Kapton-derived carbonaceous materials investigated by Kondratenko *et al.* [Reprinted with permission from Kondratenko *et al.*, J. Appl. Phys. **131**(6), 065102 (2022). Copyright 2022, American Institute of Physics].

conductance values effectively suppressed hotspot temperatures in devices with thin dielectric layers (e.g., <10 nm SiO_2), whereas high in-plane thermal conductivity values were more beneficial for thicker dielectric substrates (e.g., 300 nm SiO_2). Sun *et al.* employed the double-scan technique to characterize a self-heated Ni metal line structure fabricated on a SiO_2/Si substrate.[80] By calibrating the signal difference between contact and non-contact scans, they achieved quantitative 2D temperature mapping under ambient conditions. The method demonstrated a spatial resolution of ~45 nm and a thermal resolution of ~0.2 K. The results revealed the evolution of hotspot positions within the Ni channel as a function of applied current, as well as localized thermal accumulation associated with morphological features, as shown in Fig. 4(b).

In addition to varying the probe contact conditions, researchers have explored alternative forms of dual-scan techniques, such as switching the heat source on and off. Ramiandrisoa *et al.* systematically investigated the influence of laser modulation on thermoelectric probe-based measurements, revealing that conventional laser illumination induced measurement deviations ranging from 14% to 37% compared to dark-mode conditions, primarily attributed to laser-induced overheating.[81] Menges *et al.* compared scanning thermal resistance images of heated and unheated silicon nanowire samples to extract local temperature rises through a calibrated heat flux model.[82] They first analyzed the baseline thermal resistance state (R_{ts}) of the probe–sample system on the unheated nanowire, which was calculated using Eq. (25). The temperature rise after heating of the sample was then obtained via Eq. (26). The schematic of the tip–surface arrangement under different operation states is shown in Fig. 4(c),

$$R_{ts} = \frac{(T_{heater} - RT)}{\dot{Q}_{ts}}, \tag{25}$$

$$\Delta T_{sample} = (T_{heater} - RT)\left(1 - \frac{R_{ts}}{R'_{ts}}\right). \tag{26}$$

Here, $\dot{Q}_{ts}$ is the heat flux through the tip–sample interface and R'_{ts} is the effective thermal resistance between the probe and the sample under local temperature rise conditions. This approach enabled quantitative thermal imaging of nanowires and their junction hotspots, and notably, it provided the first direct observation of spatial shifts in hotspot location within a working nanoscale device.

The double-scan technique effectively eliminates the influence of probe-air heat exchange, thereby enhancing the quantitative accuracy of the measurement. However, its implementation requires two precisely registered scans, making it susceptible to thermal drift and topographical mismatches, which limit its applicability in dynamic environments or large-area rapid imaging. Furthermore, accurate quantitative analysis typically relies on the introduction of an empirical calibration factor, which depends on the material properties and geometry, and the thermal characteristics of the sample, which adds complexity to the calibration process.

IV. NULL-POINT METHOD

The double-scan technique relies on performing two scans under strictly identical experimental conditions. However, it is often difficult to ensure perfect consistency in scanning trajectories, environmental disturbances, and system drift. These limitations reduce its suitability for high-resolution or long-duration imaging. To overcome this constraint, researchers have developed the null-point method, which infers the sample surface temperature by adjusting the probe heating power such that the probe temperatures in the contact and non-contact modes converge. This approach eliminates the need for repeated scanning, thereby enhancing the accuracy and practicality of quantitative thermal measurements. Specifically, the Null-point method involves acquiring a series of thermal signals in a single scan and fitting a curve of $(T_c - T_{nc})$ vs Tc. By extrapolating this curve to the condition where $T_c = T_{nc}$, T_s can be obtained, as described in Eq. (27). The calibration principle of NP-SThM is illustrated in Fig. 4(d),

$$T_s = T_c|_{(T_c - T_{nc}) = 0}. \tag{27}$$

The concept of null-point SThM (NP-SThM) was first proposed by Ohmyoung Kwon's group in 2011, and they employed this to characterize the thermal properties of a wide range of materials.[83] These included surface temperature measurements of electrically heated MWCNTs (a deviation of only ~2 K compared to values calculated from TCR);[84] interfacial thermal resistance between CVD-grown graphene and SiO_2 (10×10^{-8}–45×10^{-8} m^2 K/W);[85] the thermal conductivity of residue-free suspended graphene bridges (2430 ± 190 W/m K for a 3.6 μm span at 335 K);[86] the size-dependent thermal conductivity of suspended graphene disks;[87] and the temperature distribution surrounding platinum nano heaters on silicon-on-insulator substrates.[88] By systematically correlating spatial resolution with probe design parameters, they optimized the thermal and electrical performance of the probes to reduce measurement noise and enhance spatial resolution. This led to the development of the NP-SThM technique performed under vacuum (VNP-SThM),[89] which revealed that probe temperature rise exhibits a characteristic dependence on vacuum level. Notably, operating under reduced pressure enhanced the measurement sensitivity by approximately 20 times compared to ambient conditions. Using VNP-SThM, they further achieved nanoscale temperature mapping of multi-quantum wells (MQWs) in light-emitting diodes (LEDs) under strong localized radiation.[90] The heat transfer between the thermal probe scanning across the MQW and the cross section of the operating LED was illustrated in Fig. 4(e). By analyzing the temperature difference between contact and lift mode scans, they extracted the undisturbed surface temperature of the MQW region, enabling accurate thermal characterization at the nanoscale.

In addition to fundamental developments, NP-SThM has been applied to a wide range of materials and device systems. Kondratenko *et al.* employed ambient-atmosphere NP-SThM to measure the thermal conductivity of Kapton-derived carbonaceous materials.[91] The thermal image and the thermal conductivity of the local area are presented in Fig. 4(f). The results showed excellent agreement with values obtained using conventional techniques such as photothermal radiometry, flash laser analysis, and micro-Raman thermometry. Gonzalez-Casal *et al.* applied NP-SThM to investigate the thermal conductance of self-assembled monolayer molecular junctions based on benzo[b]thiophene (BTBT) and alkylated derivatives (C8-BTBT-C8) on gold substrates, measuring per-molecule

TABLE VI. Probe type and measurement mode in each calibration strategy.

Calibration strategy	Probe	Mode
ITEC	Thermocouple/Thermistor	CCM
ETEC	Thermocouple/Thermistor	CCM
Double-scan	Thermocouple	TCM
Null-point	Thermocouple	TCM

thermal conductances of 15 and 8.8 pW/K, respectively.[92] Harnack *et al.* used NP-SThM for nanoscale temperature mapping of HfO_2-based resistive random-access memory devices, successfully visualizing localized hotspots and extracting the effective heat source size by evaluating thermal confinement and crosstalk effects.[93] FEA and harmonic signal analysis were employed to validate the measurement reliability, revealing the dominant role of thermal boundary resistance.

NP-SThM offers improved experimental stability and simplified operation. However, its accuracy relies on the precise control of probe temperature and the assumption of linearity in the fitting curve. Moreover, it is not well-suited for real-time measurements under dynamic thermal processes or rapidly varying temperature conditions. Similar to the double-scan technique, NP-SThM depends on the probe's ability to directly sense temperature and compare the thermoelectric potential between contact and non-contact states. Both methods apply primarily to thermocouple-type probes capable of voltage output and are restricted to TCM modes, where local temperature mapping is the primary objective.

To sum up, ITEC enables rapid semi-quantitative analysis by comparing signals with reference samples, but it relies on empirical fitting with limited accuracy. ETEC establishes a quantitative relationship between signal and thermal conductivity based on physical heat conduction models, offering high precision but requiring rigorous modeling and multi-sample calibration. The double-scan technique effectively eliminates non-contact artifacts and is suitable for local temperature measurements, though it demands high scan-to-scan stability. The null-point method enhances temperature measurement stability by adjusting probe power to equalize contact and non-contact signals, but it does not apply to dynamic processes or thermal conductivity quantification. Table VI summarizes the types of probes and measurement modes suited to each calibration strategy.

V. INTEGRATED INSTRUMENT

Integrated instruments in standardized SThM systems refer to setups enhanced through the incorporation of additional modules or structural optimization of the sensing unit, aimed at improving the quantitative measurement capabilities. This section focuses on representative advances categorized into three directions: (1) incorporation of multi-harmonic detection schemes such as 3ω-SThM to improve the signal-to-noise ratio and sensitivity to thermal conductivity; (2) design of integrated calibration modules that enable *in situ* or real-time correction of thermal transport parameters; and (3) optimization of thermal probe, including geometry and material composition, to minimize parasitic heat loss and enhance spatial and thermal resolution.

A. 3ω-SThM

The 3ω measurement technique is a dynamic thermal characterization method primarily used to determine the thermal conductivity of materials, which was first proposed by David G. Cahill and Robert O. Pohl in 1987.[94] In this approach, an alternating current at angular frequency ω is passed through a metal heater line deposited on the sample surface, causing Joule heating at 2ω. This periodic heating induces a temperature oscillation in the sample, which in turn modulates the heater's resistance and generates a voltage component at 3ω. By analyzing the amplitude and phase of the 3ω voltage signal, Eq. (28), the thermal properties of the underlying material can be quantitatively extracted with high sensitivity. When integrated with SThM, the 3ω technique enables localized thermal conductivity measurements by using the SThM probe as both a heater and a temperature sensor,

$$V(t) = I_0 R_0 e^{iwt} + I_0 C_0 e^{i3wt}. \tag{28}$$

Here, $V(t)$ is the time-dependent voltage response, I_0 is the peak value of the applied AC, R_0 is the reference resistance of the probe at the reference temperature, C_0 is the constant representing the amplitude of resistance modulation, $e^{i\omega t}$ represents the main frequency component representing the additional current or voltage, and $e^{i3\omega t}$ represents the 3ω component generated by the probe resistance being modulated by temperature and coupled with the 1ω current, which is the key signal source for extracting the thermal information.

Lefèvre and Volz first employed the 3ω method in SThM measurement to elucidate the limitations of conventional thermal strip techniques, Fig. 5(a).[95] Through experimental calibration, they determined key thermal contact parameters between the probe and the sample. Equation (29) establishes the direct relationship between the sample thermal conductivity (K_s) with the heat flux density (σ_S),

$$s_S = 2k_S \pi b \theta_0 \left(1 + b\sqrt{\frac{2i\omega}{a_S}}\right). \tag{29}$$

Here, θ_0 is the temperature amplitude, b is the contact radius, and a_s is the sample thermal diffusivity. They determined the precise calibration of probe geometric parameters via the AC mode, which reduces measurement uncertainty by four orders of magnitude and extends the detectable thermal conductivity range from insulators to highly conductive materials. Chirtoc *et al.* employed SThM with a resistive Wollaston thermal probe to investigate local variations in thermal conductivity in NiTi microstructures during the martensitic-to-austenitic phase transition.[96] By modeling the 3ω signal using a lumped thermal model analogous to a first-order low-pass electrical circuit, they identified a cutoff frequency that depends on the thermal conductivity of the sample and proposed the following Eq. (30) to calculate the thermal conductivity change. The approach was combined with a novel dual-normalization data processing method that effectively eliminated temperature drift

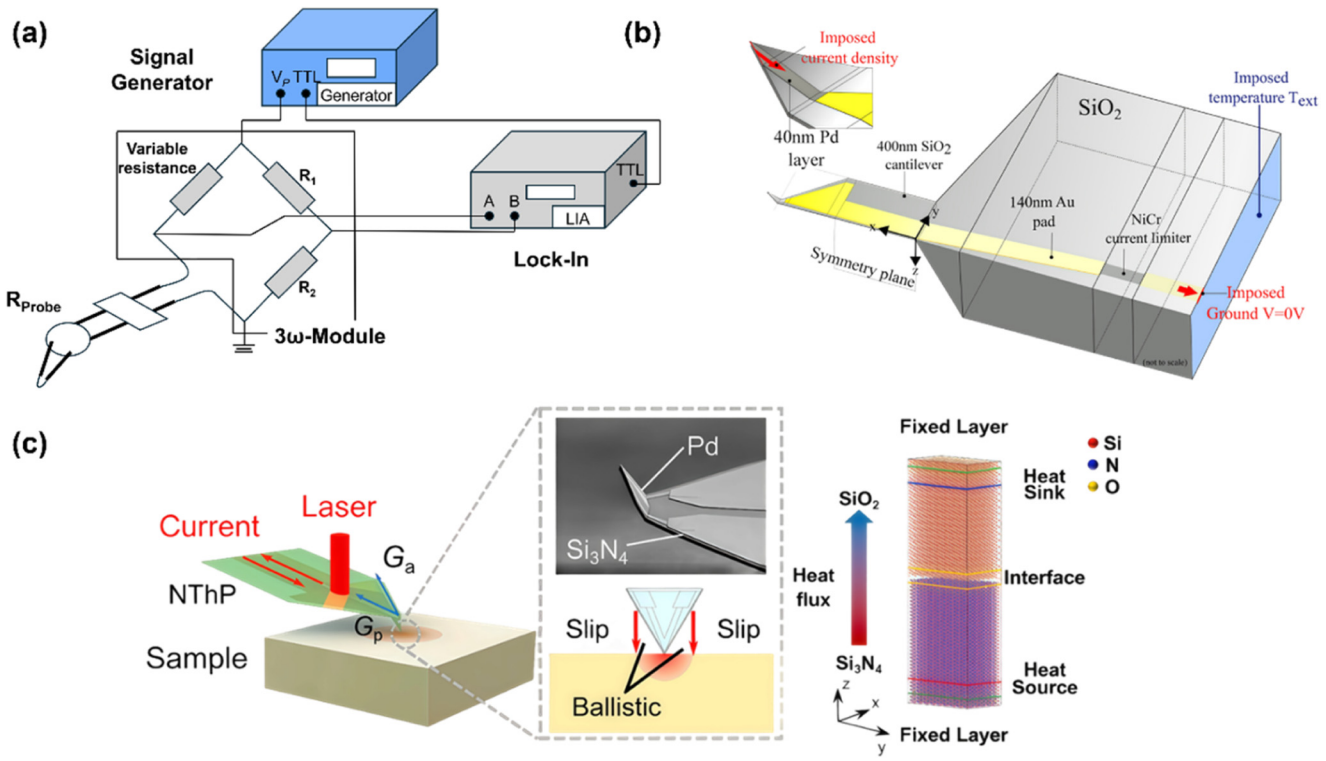

FIG. 5. (a) The experimental setup of 3ω-SThM proposed by Lefèvre and Volz [Reprinted with permission from Lefèvre and Volz Rev. Sci. Instrum. **76**(3), 033701 (2005). Copyright 2005, American Institute of Physics]. (b) The 3D geometry built for FEA in 3ω-SThM by Pernot *et al.* [Reprinted with permission from Pernot *et al.*, J. Appl. Phys. **129**, 055105 (2021). Copyright 2021, American Institute of Physics]. (c) The principle of deconvolution in 3ω signals and the simulated cell structure by NEMD proposed by Liu *et al.* [Reprinted with permission from Liu *et al.*, Int. J. Heat Mass Transfer **232**, 125979 (2024). Copyright 2024, Elsevier].

errors, enabling precise quantification of small thermal conductivity changes,

$$\frac{\Delta k}{k} = \frac{V_{nII} - 1}{S(k)}. \tag{30}$$

Here, Δk is the thermal conductivity change and k is the initial thermal conductivity. V_{nII} represents the amplitude of the 3ω signal after dual normalization processing and "1" corresponds to the reference value when there is no change in thermal conductivity, for which are normalized representations. $S(k)$ represents the sensitivity of the normalized 3ω signal to variations in the sample's thermal conductivity. It quantifies how strongly the signal responds to changes in k and directly influences the measurement's ability to resolve subtle differences in local thermal transport. High sensitivity is essential for achieving accurate and quantitative thermal imaging at the nanoscale. Leitgeb *et al.* quantitatively characterized the thermal properties of 500 nm-thick tungsten films using 3ω-SThM.[97] By establishing a relationship between the 3ω signal and thermal conductivity, they derived relevant equations from the system's heat flow model, Eq. (31). A linear fit to the plot of the 3ω signal vs the logarithm of the heating frequency allowed for the extraction of the slope, which enabled accurate determination of the thermal conductivity,

$$U_{3\omega\_1} - U_{3\omega\_2} = \frac{1}{4} I_0 \frac{dR}{dT}\left(\frac{1}{k_s}\frac{P}{p}[\ln(\omega_1) - \ln(\omega_2)]\right). \tag{31}$$

Here, $U_{3\omega}$ is the third-harmonic voltage signal, I_0 is the current applied to the thermal probe, dR/dT represents the temperature coefficient of the probe resistance, and P is the heating power. Trefon-Radziejewska *et al.* investigated the thermal transport properties of CuPc thin films using 3ω-SThM.[98] By analyzing the measured signals and constructing a calibration curve based on reference materials with known thermal conductivities, they estimated the thermal conductivity of the CuPc films. The results were further corrected through thermal spreading resistance analysis to account for the influence of the substrate's thermal properties.

3ω-SThM is often combined with modeling approaches such as FEM to accurately simulate the complex heat exchange processes at the probe–sample interface and to provide a physical interpretation of the third-harmonic signals. Altes *et al.* were among the first to propose the integration of 3ω-SThM with FEA for quantitative measurements.[99] By constructing a 3D FEM to simulate the

thermal response of the probe under periodic electrical heating, they implemented a two-step calibration strategy to comprehensively characterize the thermal behavior of the probe itself, laying the groundwork for accurate interfacial heat flux inversion. Pernot *et al.* further enhanced the quantitative capabilities of the method.[100] They performed DC and AC electrical calibration of the SThM probe under non-contact conditions and then fitted the experimentally acquired 3ω signals with FEA results. By iteratively tuning interfacial parameters in the model, they successfully extracted the interfacial thermal resistance between the probe and the sample. The schematic of the 3D FEA used for 3ω-SThM analysis is shown in Fig. 5(b). Liu *et al.* applied 3ω-SThM to measure the thermal boundary resistance at Si_3N_4/SiO_2 nanoheterojunctions.[101] They developed a dual-channel heat flux model capable of decoupling total and contact thermal conductance and incorporated both Joule heating and laser heating in the modeling framework. This allowed the deconvolution of interfacial contributions directly from the measured 3ω signal. Notably, the experimental results were compared against NEMD simulations performed using the LAMMPS (large-scale atomic/molecular massively parallel simulator) platform, with the embedded atom method used to model interfacial temperature differences and atomic-scale interactions. The resulting $R_{boundary}$ differed from experimental results by only 2.8%, validating the accuracy and theoretical robustness of the 3ω-SThM&MD approach for nanoscale interfacial thermal measurements. Figure 5(c) illustrates the deconvolution principle of the 3ω signal and the simulated cell structure used in the NEMD analysis.

3ω-SThM enables localized thermal conductivity measurements with sub-100 nm resolution, making it suitable for characterizing spatially inhomogeneous or structured materials. Additionally, by adjusting the modulation frequency, 3ω-SThM allows depth-dependent thermal probing, offering insight into vertical heterostructures and thin films. It should be noted that this technique also faces several practical challenges. It requires a relatively complex instrumentation setup, involving precise control of the AC excitation frequency, phase-locked detection using lock-in amplifiers, and often dual-modulation circuits for background noise rejection.[102] Meanwhile, it is limited by the usable frequency window: the frequency must be high enough to generate measurable 3ω signals yet low enough to remain within the quasi-steady-state approximation of the thermal diffusion model.[103] Additionally, the thermal time constant of the probe and the signal-to-noise ratio of the 3ω component place further constraints on the operable frequency range.

B. Integrated with calibration modules

The integration of additional calibration modules into SThM serves as a key strategy for enabling quantitative analysis and improved testing accuracy. The core principle lies in transforming originally qualitative thermal images into data with physical meaning (such as absolute temperature or thermal conductivity) through standardized reference systems and thermal response modeling. These calibration modules can be integrated into the probe itself or implemented on the testing sample substrate.

Incorporating additional modules at the probe for temperature and heat flux calibration is a commonly employed approach. Janus *et al.* introduced an active microdevice into the thermal probe, consisting primarily of a thin-film platinum micro-resistor embedded within a 100 nm-thick SiO_2 layer, with the detailed fabrication process presented in Fig. 6(a).[104] The device provides a controllable and uniform temperature field for SThM as a calibration standard, effectively eliminating parasitic edge effects and enhancing measurement accuracy and stability. The four-probe electrode configuration allows precise temperature modulation, achieving a temperature resolution of 50 mK and an electrical temperature measurement accuracy as high as 1×10^{-6}. Reihani *et al.* integrated a thin-film platinum resistor at the apex of the probe, functioning as both a heater and a temperature sensor.[105] This configuration enabled simultaneous measurement of the probe response and the probe–sample thermal contact resistance, allowing for the decoupling of error components within the thermal signal and facilitating accurate temperature extraction. By combining modulated heating with dual-channel temperature response acquisition (DC + AC), they developed a thermal network model to quantitatively determine both the sample surface temperature and the contact resistance. They claimed that this design effectively suppressed measurement artifacts caused by surface topography, tip wear, or thermal drift, achieving a temperature resolution of approximately 50 mK and a spatial resolution of ∼7 nm.

Another approach is the use of substrate-integrated calibration modules, in which miniature heaters or temperature sensors are embedded within the sample substrate or test structure to serve as known reference elements. Nguyen *et al.* introduced a microthermal chip with an integrated thermal sensor for calibration.[106] The device features a suspended thin-film structure incorporating a 50 μm-diameter heating resistor and a 10 μm-diameter resistance temperature detector (RTD) positioned at the center of the membrane, Fig. 6(b), enabling high-precision and accurate measurement. Dawson *et al.* integrated a MEMS-based heating platform to deliver thermal pulses, Fig. 6(c), while the thermal probe was used to measure the temperature at the top surface of the test thin film.[107] The recorded temperature evolution corresponded to voltage changes. By fitting the data with an exponential decay curve, the time required to reach half of the maximum temperature rise ($t_{1/2}$) was extracted. The thermal diffusivity (α) is related to film thickness (d) and $t_{1/2}$, calculated by Eq. (32),

$$\alpha = 0.1398 \cdot \frac{d^2}{t_{1/2}}. \tag{32}$$

The constant 0.1398 is a numerical solution derived from the idealized adiabatic heat conduction model of a homogeneous slab.[108] Umatova *et al.* developed a MEMS-based silica membrane device integrated with thermal sensors, fabricated using high-precision nanofabrication techniques including electron beam lithography and dry etching.[109] The system incorporates Pt–Au thermocouples and RTDs, which serve both as heaters and as highly sensitive temperature sensors, Fig. 6(d), enabling high spatial resolution and thermal responsiveness.

Another strategy is integrating external optical or electronic sensors with the probe system to obtain additional thermal field or heat flux information. Chirtoc *et al.* proposed a heat flux sharing and thermal conductivity calibration method for SThM by combining a

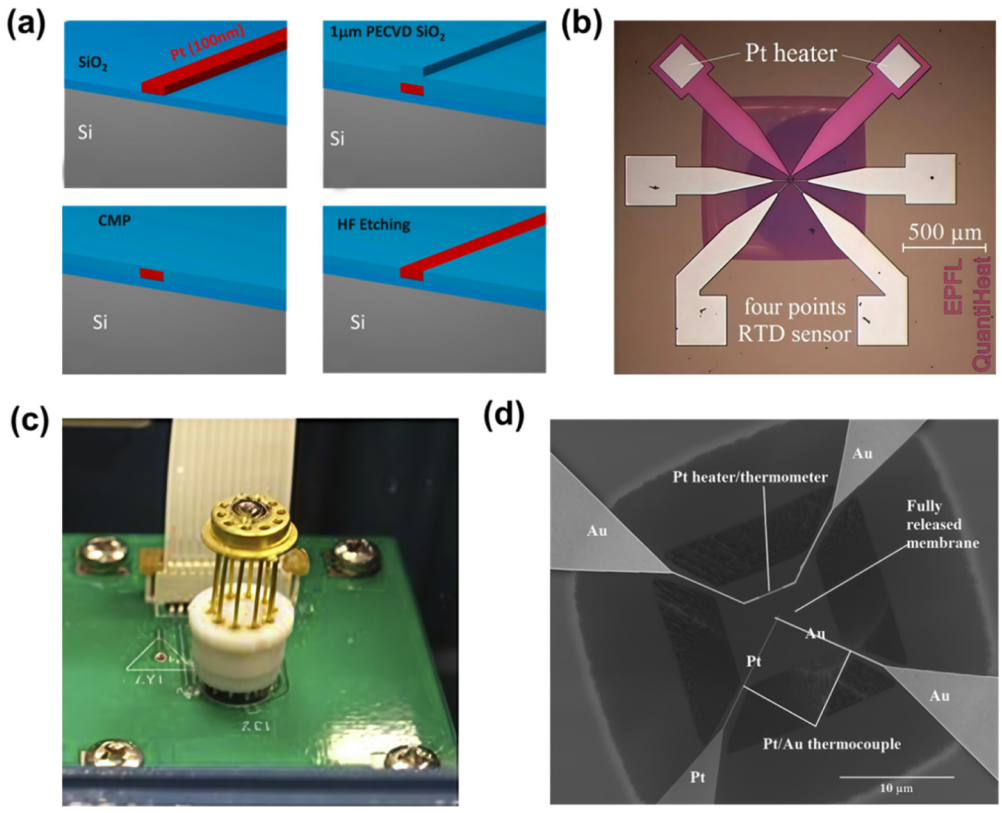

FIG. 6. (a) Fabrication process of the specifically designed thermal probe designed by Janus *et al*. [Reprinted with permission from Janus *et al*., Ultramicroscopy **221**, 113188 (2021). Copyright 2020, Elsevier]. (b) The optical image of the introduced calibration chips designed by Nguyen *et al*. [Reprinted with permission from Nguyen *et al*., J. Heat Transfer **141**, 071601 (2019). Copyright 2019, ASME]. (c) Illustration of the MEMS heater device designed by Dawson *et al*. [Reprinted with permission from Dawson *et al*., Polym. Test. **41**, 198–208 (2015). Copyright 2015, Elsevier]. (d) SEM image of the MEMS-based silica membrane device integrated with Pt heater-resistance thermometer elements and Pt–Au thermocouples designed by Umatova *et al*. [Reprinted with permission from Umatova *et al*., Rev. Sci. Instrum. **90**, 095003 (2019). Copyright 2019, American Institute of Physics.].

resistive thermal probe with a piezoelectric heat flux sensor (PES).[110] The PES enables precise measurement of the actual heat flux transferred from the probe into the sample, and it can be used to distinguish the individual contributions of conductive, radiative, and convective heat transfer under various configurations (vacuum/air environments and contact/non-contact modes). The distribution of heat flux under contact and non-contact conditions is described by Eq. (33). In this specific experimental configuration, they found that approximately 60% of the input power dissipated through the cantilever, while about 19.5% was transferred through the tip–sample contact. However, it should be noted that these values are highly system-specific and strongly influenced by probe geometry, contact area, and material thermal properties,

$$\frac{G_{sc}}{G_{sa}^{N,C}} = \frac{V_{2\omega}^{C}}{V_{2\omega}^{N}}\frac{G^{C}}{G^{N}} - 1 = \frac{V_{2\omega}^{C}}{V_{2\omega}^{N}}\frac{V_{3\omega}^{N}}{V_{3\omega}^{C}} - 1. \tag{33}$$

Here, $V_{2\omega}^{C}$ and $V_{2\omega}^{N}$ denote the 2ω signals under contact and non-contact conditions, respectively. G^{N} and G^{C} are the total thermal conductance under non-contact and contact states. G_{sc} refers to the thermal conductance through the contact interface, while G_{sa} corresponds to the thermal conductance through air. Nguyen *et al*. introduced two types of micro-heater platforms for calibration: a micro-heating plate integrated with a local RTD and an optical thermal imaging device (OPT) based on a separate platinum film.[111] The RTD was used to monitor local temperature changes in real time during probe–sample contact, while the OPT employed near-infrared thermal imaging to visualize perturbations in the membrane's temperature distribution upon contact. By capturing real-time thermal images before and after probe contact, the spatial extent and characteristics of the temperature disturbance were analyzed to estimate the local heat flux distribution. It enables the quantification of probe-induced thermal flux variations and allows for spatial calibration of the probe response and thermal conductivity mapping when combined with FEA. Ge *et al*. developed a micro/nanoscale heating platform based on Johnson noise thermometry, enabling programmable control of the heating zone size and providing highly uniform thermal calibration.[112] The interfacial thermal resistance was quantitatively determined by numerically solving the established 1D heat transfer equation.

Additional integration strategies have also been explored. Pruchnik *et al.* designed a system in which a low-frequency transformer bridge metrology module is integrated within the external microcontroller-based control circuitry and the preamplifier board.[113] By employing a 1 kHz AC drive and microprocessor-controlled direct digital synthesis voltage regulation, the system effectively suppressed parasitic capacitive interference, achieving a temperature resolution of 0.6 mK and a sensitivity of 5 mV/K. The developed platform offers electrical isolation to minimize self-heating effects and reduce measurement noise. Additionally, the quality of thermal imaging can be quantitatively assessed using the information channel capacity method.

The integration of calibration modules significantly enhances measurement repeatability, sensitivity, and quantitative accuracy. This approach is particularly well-suited for applications such as thermal conductivity mapping and interfacial thermal resistance extraction. Its key advantages include enabling *in situ* calibration, error control, and standardization of heat flux pathways. However, it is important to emphasize that this strategy is currently feasible only on self-built SThM platforms. Commercial SPMs often lack the flexible electrical interfaces and mechanical compatibility required to accommodate such modifications. Moreover, integrating a calibration module at the probe is only appropriate for resistive probes equipped with metal strip resistors, such as KNT-type probes. Therefore, while these integrated calibration strategies significantly enhance measurement precision, their practical application remains largely limited to custom-designed systems rather than off-the-shelf instruments.

C. Cantilever and probe optimization

Cantilever and probe optimization focuses on improving the thermal design of the cantilever and probe to enhance sensitivity to local temperature rises and ensure signal stability. By guiding heat flow predominantly along the probe–sample path, these optimizations enable the measured temperature signal to more accurately reflect the sample's thermal conductivity or interfacial thermal resistance, thereby facilitating quantitative thermal measurements.

McConney *et al.* proposed a twisting bimorph cantilever design for quantitative measurements with high spatial resolution and temperature sensitivity.[114] By constructing an asymmetric bi-material structure on a V-shaped cantilever, the thermal response is manifested as lateral twisting rather than vertical bending. Figure 7(a) presents the comparison of the normal mode and the twisting mode. This design enables complete decoupling of the thermal signal channel from the topographical imaging channel. They successfully utilized the lateral deflection signal to capture thermal responses while retaining vertical deflection for surface topography imaging, allowing for quantitative observation of contrast inversion induced by changes in thermal conductivity. The device demonstrated a thermal sensitivity of up to 65.4 mV/K, a thermal resolution of 27 mK, and a spatial resolution of 0.61 nm, representing an improvement of two orders of magnitude over conventional SThM systems. Janus *et al.* reported a novel micromachined test structure designed for optimized SThM cantilevers.[115] The structure consists of four independently controlled platinum microheaters embedded in a 500 nm-thick Si/Si_3N_4 membrane, Fig. 7(b), enabling precise control of both the temperature distribution and heat flux at the probe–sample contact interface. Through thermoelectric calibration and accurate load control, a quantitative relationship was established between the probe output signal and the actual temperature, thereby enabling accurate thermal conductivity measurements.

Yang *et al.* considered multi-asperity contact between the probe and the sample and proposed a tip–surface contact model alongside a thin-plate model for probe optimization.[116] Hwang *et al.* improved the performance of SThM probes by refining hard mask design and etching processes, which reduced the tip radius to 50 nm and the thermocouple junction diameter to 100 nm.[117] It significantly increased the sensitivity and spatial resolution, while also enhancing the repeatability, uniformity, and yield of the batch fabrication process. Chae *et al.* developed a novel thermal probe by engineering the tip with an ultrathin oxide layer (~100 nm), leveraging the mechanical stability of micromachined structures even at minimal film thickness.[118] Figure 7(c) illustrates the comparison of the common probe and the optimized probe. The new design reduced the tip radius substantially, decreased the thermal time constant from 0.56 to 0.15 ms, and increased the thermal sensitivity from 1.33 to 1.85 K/μW. Janus *et al.* reported a 3D platinum nanostructured tip employing both the heat source and temperature sensor.[119] The tip curvature radius was further sharpened to less than 100 nm through FIB post-processing [Fig. 7(d)]. The piezoresistive bridge configuration enabled precise measurement of both mechanical deformation and thermal response, thereby eliminating the optical detection interference typically associated with thermal measurements. Hirotani *et al.* designed a carbon nanotube (CNT)-based thermal probe by attaching a single CNT to a suspended platinum membrane, which served simultaneously as both a heater and a temperature sensor.[120] By precisely controlling Joule heating in the platinum membrane, the temperature at the CNT-sample contact point was matched to the sample surface temperature. Based on the heat transfer model described in Fig. 7(e), they use a pre-calibrated resistance–temperature relationship to extract the sample surface temperature, effectively eliminating errors associated with thermal contact resistance. Timofeeva *et al.* demonstrated quantitative measurements of thermal conductivity and interfacial thermal resistance by integrating highly thermal conductive nanowires (specifically multiple-wall carbon nanotubes, MWCNTs) into the apex of the thermal probe.[121] They claimed that MWCNT-based probes significantly reduced the thermal contact resistance, improving thermal coupling efficiency with highly thermal conductive materials such as aluminum and graphene. Nam *et al.* coated the apex of the thermal probe with a thin layer of graphene oxide (GO).[122] Owing to the high photothermal conversion efficiency and electrical resistivity, the incorporation of GO significantly improved the thermal response of the probe to laser irradiation, Fig. 7(f). Without significantly increasing the probe size, it increased the intensity of the photothermal signal by an average of 1.76 times and the optical contrast of the image by 2.56 times.

One important aspect that should be mentioned is the relationship between tip sharpening and the improvement of spatial resolution in thermal measurements. While sharpened or nanofabricated tips are often pursued to enhance spatial resolution

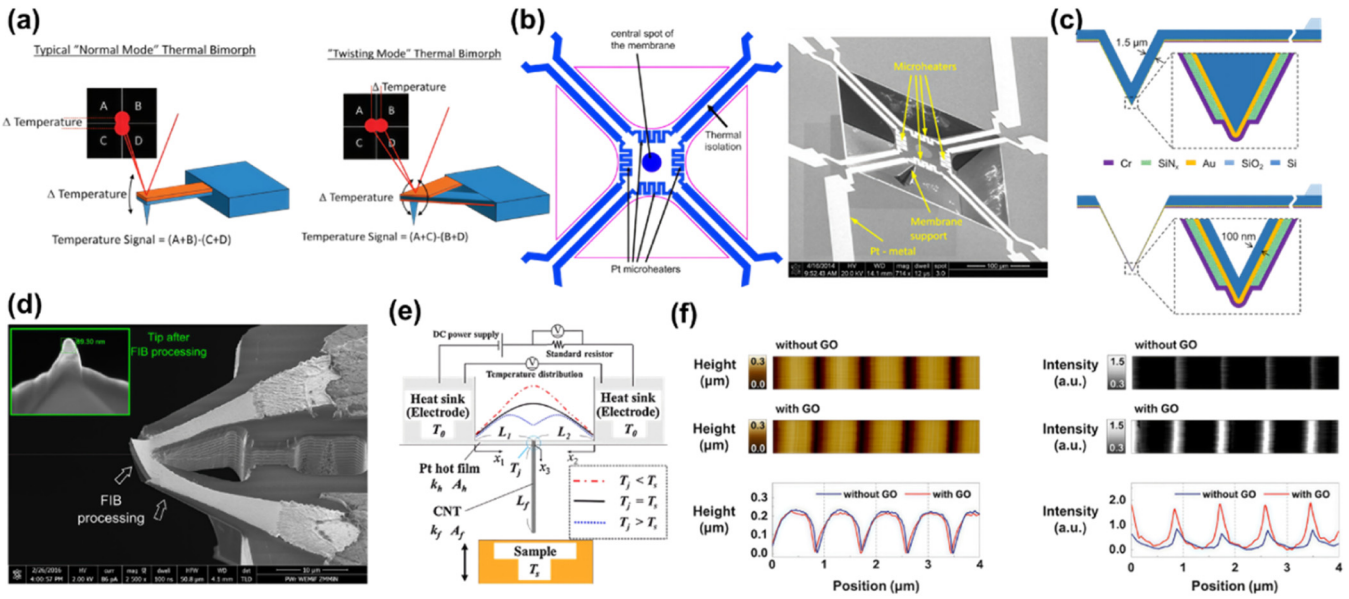

FIG. 7. (a) Comparison of the normal mode and twisting mode proposed by McConney *et al.* [Reprinted with permission from McConney *et al.*, Nano Lett. **12**, 1218–1223 (2012). Copyright 2012, American Chemical Society]. (b) The design of the novel micromachined test structure and the corresponding SEM image by Janus *et al.* [Reprinted with permission from Janus *et al.*, Microelectronic Eng. **174**, 70–73 (2017). Copyright 2017, Elsevier]. (c) Comparison of common NP probe and NP probe with extremely thin oxide films by Chae *et al.* [Reprinted with permission from Chae *et al.*, Ultramicroscopy **171**, 195–203 (2016). Copyright 2016, Elsevier]. (d) SEM images of the tip sharpened by FIB milling down to 100 nm by Janus *et al.* [Reprinted with permission from Janus *et al.*, Ultramicroscopy **193**, 104–110 (2018). Copyright 2018, Elsevier]. (e) Heat transfer model of a suspended platinum hot film with a single CNT probe by Hirotani *et al.* [Reprinted with permission from Hirotani *et al.*, Sens. Actuators A, Phys. **199**, 1–8 (2013). Copyright 2013, Elsevier]. (f) The scanned topography and optical images by the thermal probe coated and uncoated GO layer along with the height and intensity profile by Nam *et al.* [Reprinted with permission from Nam *et al.*, Appl. Phys. Lett. **122**, 213505 (2023). Copyright 2023, American Institute of Physics.].

(realizing temperature mapping at the nanoscale in TCM), it is important to note that such miniaturization may not be optimal for CCM. In CCM, the measurable signal depends strongly on the magnitude of tip–sample heat flux. A reduced contact area inherently limits thermal coupling, thereby diminishing the sensitivity to local thermal conductivity variations. This introduces a trade-off between spatial resolution and signal robustness. As such, the design of thermal probes should consider this balance and optimization strategies should be tailored to the specific measurement mode and target application.

VI. CONCLUSIONS

In this review, the authors have comprehensively discussed the theoretical basis and experimental strategies for nanoscale thermal transport characterization using SThM. This discussion is structured around three core areas: theoretical modeling, the evolution of calibration strategies, and the optimization of probe-system integration. In Sec. II, the multi-channel heat transfer mechanisms at the probe–sample interface are systematically clarified along with the corresponding analytical models, thereby establishing a foundation for understanding and quantifying interfacial thermal resistance. In terms of calibration strategies, the progression from basic temperature sensor calibration (RPTC) to ITEC, ETEC, the double-scan technique, and the null-point method is reviewed, reflecting a shift from empirical fitting to physics-based modeling approaches. For system integration, key advancements are summarized, including the development of 3ω-SThM, the incorporation of integrated calibration modules, and the structural refinement of cantilevers and probes. These innovations collectively improve thermal stability, measurement sensitivity, and the reliability of quantitative thermal analysis.

Looking ahead, key challenges remain in achieving high-fidelity, quantitative SThM measurements due to probe–sample interaction uncertainty, heat spreading effects, and reliance on multi-parameter calibration. Future directions include: (i) integrating multi-physics modeling (mechanical, thermal, electrical), (ii) developing real-time, self-calibrating probe systems, and (iii) leveraging data-driven and machine-learning techniques (such as the employment of physics-informed neural networks for efficient partial differential equation solution) for thermal image analysis and model inversion. By addressing these challenges, SThM can evolve from a qualitative imaging tool into a robust platform for quantitative nanoscale thermophysics.

ACKNOWLEDGMENTS

The authors gratefully acknowledge the support provided by the National Natural Science Foundation of China (Nos. 52306214,

52327809, 52376159, and 52425601), the Shanghai Chenguang Plan Program (No. 22CGA78), and the National Key Research and Development Program of China (No. 2023YFB4404104).

AUTHOR DECLARATIONS

Conflict of Interest

The authors have no conflicts to disclose.

Author Contributions

Yifan Li: Investigation (equal); Writing – original draft (equal). **Jiang Wu:** Investigation (equal); Methodology (equal); Writing – original draft (equal). **Jing Luo:** Methodology (equal). **Jianli Wang:** Methodology (equal); Supervision (equal). **Wei Yu:** Supervision (equal). **Bingyang Cao:** Conceptualization (equal); Funding acquisition (equal); Supervision (equal); Writing – review & editing (equal).

DATA AVAILABILITY

The data that support the findings of this study are available from the corresponding author upon reasonable request.

REFERENCES

[1]G. Chen, "Non-Fourier phonon heat conduction at the microscale and nanoscale," Nat. Rev. Phys. **3**, 555–569 (2021).
[2]C. Silvestri, M. Riccio, R. H. Poelma, B. Morana, S. Vollebregt, F. Santagata, A. Irace, G. Q. Zhang, and P. M. Sarro, "Thermal characterization of carbon nanotube foam using MEMS microhotplates and thermographic analysis," Nanoscale **8**, 8266–8275 (2016).
[3]Z. Y. Liu, Z. K. Liu, G. Yang, and B. Y. Cao, "Multi-pulse thermoreflectance imaging with structure function analyses for measuring thermophysical properties of microscale heterostructures," Int. J. Heat Mass Transfer **229**, 125737 (2024).
[4]M. Kuball and J. W. Pomeroy, "A review of Raman thermography for electronic and opto-electronic device measurement with submicron spatial and nanosecond temporal resolution," IEEE Trans. Device Mater. Reliab. **16**, 667–684 (2016).
[5]S. Sandell, E. Chávez-Ángel, A. El Sachat, J. He, C. M. Sotomayor Torres, and J. Maire, "Thermoreflectance techniques and Raman thermometry for thermal property characterization of nanostructures," J. Appl. Phys. **128**, 13 (2020).
[6]B. R. Burg, M. Kolly, N. Blasakis, D. Gschwend, J. Zürcher, and T. Brunschwiler, "Steady-state low thermal resistance characterization apparatus: The bulk thermal tester," Rev. Sci. Instrum. **86**, 124903 (2015).
[7]E. T. Swartz and R. O. Pohl, "Thermal resistance at interfaces," Appl. Phys. Lett. **51**, 2200–2202 (1987).
[8]F. Gucmann, J. W. Pomeroy, and M. Kuball, "Scanning thermal microscopy for accurate nanoscale device thermography," Nano Today **39**, 101206 (2021).
[9]E. Guen, P. Klapetek, R. Puttock, B. Hay, A. Allard, T. Maxwell, P.-O. Chapuis, D. Renahy, G. Davee, M. Valtr, J. Martinek, O. Kazakova, and S. Gomès, "SThM-based local thermomechanical analysis: Measurement intercomparison and uncertainty analysis," Int. J. Therm. Sci. **156**, 106502 (2020).
[10]S. Gomès, A. Assy, and P.-O. Chapuis, "Scanning thermal microscopy: A review," Phys. Status Solidi (A) **212**, 477–494 (2015).
[11]J. Park, S. Koo, and K. Kim, "Measurement of thermal boundary resistance in ~10 nm contact using UHV-SThM," Int. J. Nanotechnol. **16**, 263–272 (2019).
[12]J. Christofferson, K. Maize, Y. Ezzahri, J. Shabani, X. Wang, and A. Shakouri, "Microscale and nanoscale thermal characterization techniques," Sens. Actuators, A **130**, 041101 (2008).
[13]Y. Li, Y. Zhang, Y. Liu, H. Xie, and W. Yu, "A comprehensive review for micro/nanoscale thermal mapping technology based on scanning thermal microscopy," J. Therm. Sci. **31**, 976–1007 (2022).
[14]C. Williams and H. Wickramasinghe, "Scanning thermal profiler," Microelectron. Eng. **5**, 509–513 (1986).
[15]E. Gmelin, R. Fischer, and R. Stitzinger, "Sub-micrometer thermal physics–An overview on SThM techniques," Thermochim. Acta **310**, 1–17 (1998).
[16]G. Wielgoszewski and T. Gotszalk, "Scanning thermal microscopy (SThM): How to map temperature and thermal properties at the nanoscale," Adv. Imaging Electron Phys. **190**, 177–221 (2015).
[17]Y. Zhang, W. Zhu, F. Hui, M. Lanza, T. Borca-Tasciuc, and M. Muñoz Rojo, "A review on principles and applications of scanning thermal microscopy (SThM)," Adv. Funct. Mater. **30**, 1900892 (2020).
[18]J. Bodzenta and A. Kaźmierczak-Bałata, "Scanning thermal microscopy and its applications for quantitative thermal measurements," J. Appl. Phys. **132**, 140902 (2022).
[19]J. Bodzenta, A. Kaźmierczak-Bałata, and K. Harris, "Quantitative thermal measurement by the use of scanning thermal microscope and resistive thermal probes," J. Appl. Phys. **127**, 031103 (2020).
[20]L. Dong and Y. Li, "Experimental identification of topography-based artifact phenomenon for micro-/nanoscale thermal characterization of polymeric materials in scanning thermal microscopy," AIP Adv. **12**, 045311 (2022).
[21]A. Assy, S. Lefèvre, P.-O. Chapuis, and S. Gomès, "Analysis of heat transfer in the water meniscus at the tip-sample contact in scanning thermal microscopy," J. Phys. D: Appl. Phys. **47**, 442001 (2014).
[22]L. Shi and A. Majumdar, "Thermal transport mechanisms at nanoscale point contacts," J. Heat Transfer **124**, 329–337 (2002).
[23]Z. M. Zhang, Z. M. Zhang, and Luby, *Nano/Microscale Heat Transfer* (Springer, 2007), Vol. 410, p. 761.
[24]M. Wang, N. Yang, and Z.-Y. Guo, "Non-Fourier heat conductions in nanomaterials," J. Appl. Phys. **110**, 064310 (2011).
[25]V. Bhosle, J. Prater, F. Yang, D. Burk, S. Forrest, and J. Narayan, "Gallium-doped zinc oxide films as transparent electrodes for organic solar cell applications," J. Appl. Phys. **102**, 023501 (2007).
[26]G. A. Bird, *Molecular Gas Dynamics and the Direct Simulation of Gas Flows* (Oxford University, 1994).
[27]A. I. Zhmakin, *Non-Fourier Heat Conduction* (Springer, Cham, 2023).
[28]A. R. Peeketi, M. Moscardini, S. Pupeschi, Y. Gan, M. Kamlah, and R. K. Annabattula, "Analytical estimation of the effective thermal conductivity of a granular bed in a stagnant gas including the Smoluchowski effect," Granul. Matter **21**, 1–21 (2019).
[29]J. C. Cuevas and F. J. García-Vidal, "Radiative heat transfer," ACS Photonics **5**, 3896–3915 (2018).
[30]A. Volokitin and B. N. Persson, "Near-field radiative heat transfer and noncontact friction," Rev. Mod. Phys. **79**, 1291–1329 (2007).
[31]S.-A. Biehs, R. Messina, P. S. Venkataram, A. W. Rodriguez, J. C. Cuevas, and P. Ben-Abdallah, "Near-field radiative heat transfer in many-body systems," Rev. Mod. Phys. **93**, 025009 (2021).
[32]D. Polder and M. Van Hove, "Theory of radiative heat transfer between closely spaced bodies," Phys. Rev. B **4**, 3303 (1971).
[33]A. Yuffa, P. Martin, and J. Scales, "Scattering from a large cylinder with an eccentrically embedded core: An orders-of-scattering approximation," J. Quant. Spectrosc. Radiat. Transfer **133**, 520–525 (2014).
[34]A. Taflove, "The finite difference time domain method," Comput. Electromagn. **3**, 629–670 (2005).
[35]A. G. Polimeridis, M. H. Reid, W. Jin, S. G. Johnson, J. K. White, and A. W. Rodriguez, "Fluctuating volume-current formulation of electromagnetic fluctuations in inhomogeneous media: Incandescence and luminescence in arbitrary geometries," Phys. Rev. B **92**, 134202 (2015).
[36]A. W. Rodriguez, M. H. Reid, and S. G. Johnson, "Fluctuating-surface-current formulation of radiative heat transfer: Theory and applications," Phys. Rev. B **88**, 054305 (2013).

[37]P. Kapitza, "Heat transfer and superfluidity of helium II," Phys. Rev. **60**, 354 (1941).
[38]J. Chen, X. Xu, J. Zhou, and B. Li, "Interfacial thermal resistance: Past, present, and future," Rev. Mod. Phys. **94**, 025002 (2022).
[39]H. Bao, J. Chen, X. Gu, and B. Cao, "A review of simulation methods in micro/nanoscale heat conduction," ES Energy Environ. **1**, 16–55 (2018).
[40]D. G. Cahill, W. K. Ford, K. E. Goodson, G. D. Mahan, A. Majumdar, H. J. Maris, R. Merlin, and S. R. Phillpot, "Nanoscale thermal transport," J. Appl. Phys. **93**, 793–818 (2003).
[41]D. Young and H. Maris, "Lattice-dynamical calculation of the Kapitza resistance between fcc lattices," Phys. Rev. B **40**, 3685 (1989).
[42]V. M. Nazarychev, A. D. Glova, I. V. Volgin, S. V. Larin, A. V. Lyulin, S. V. Lyulin, and A. A. Gurtovenko, "Evaluation of thermal conductivity of organic phase-change materials from equilibrium and non-equilibrium computer simulations: Paraffin as a test case," Int. J. Heat Mass Transfer **165**, 120639 (2021).
[43]J.-L. Barrat and F. Chiaruttini, "Kapitza resistance at the liquid-solid interface," Mol. Phys. **101**, 1605–1610 (2003).
[44]J.-S. Wang, J. Wang, and N. Zeng, "Nonequilibrium green's function approach to mesoscopic thermal transport," Phys. Rev. B **74**, 033408 (2006).
[45]B. Hu, W. Bao, G. Chen, Z. Wang, and D. Tang, "Boltzmann transport equation simulation of phonon transport across GaN/AlN interface," Comput. Mater. Sci. **230**, 112485 (2023).
[46]Y. Li, H. Lin, and N. Mehra, "Identification of thermal barrier areas in graphene oxide/boron nitride membranes by scanning thermal microscopy: Thermal conductivity improvement through membrane assembling," ACS Appl. Nano Mater. **4**, 4189–4198 (2021).
[47]Y. Li, N. Mehra, T. Ji, X. Yang, L. Mu, J. Gu, and J. Zhu, "The stiffness-thermal conduction relationship at the composite interface: the effect of particle alignment on the long-range confinement of polymer chains monitored by scanning thermal microscopy," Nanoscale **10**, 1695–1703 (2018).
[48]J. A. Mittereder, J. A. Roussos, W. T. Anderson, and D. E. Ioannou, "Quantitative measurement of channel temperature of GaAs devices for reliable life-time prediction," IEEE Trans. Reliab. **51**, 482–485 (2002).
[49]P. G. Weber, C. C. Borel, W. B. Clodius, B. J. Cooke, and B. W. Smith, Proc. SPIE **3701**, 144–154 (1999).
[50]E. R. Meinders, "Measurement of the thermal conductivity of thin layers using a scanning thermal microscope," J. Mater. Res. **16**, 2530–2543 (2001).
[51]A. A. Wilson, "Scanning thermal probe calibration for accurate measurement of thermal conductivity of ultrathin films," MRS Commun. **9**, 650–656 (2019).
[52]N. Fleurence, S. Demeyer, A. Allard, S. Douri, and B. Hay, "Quantitative measurement of thermal conductivity by SThM technique: Measurements, calibration protocols and uncertainty evaluation," Nanomaterials **13**, 2424 (2023).
[53]V. Leitgeb, R. Hammer, L. Mitterhuber, K. Fladischer, F. Peter, A. Buerke, and S. Defregger, "Thermal and spatial resolution in scanning thermal microscopy images: A study on the probe's heating parameters," J. Appl. Phys. **129**, 164502 (2021).
[54]L. Zheng, T. Zhu, Y. Li, H. Wu, C. Yi, J. Zhu, and X. Gong, "Enhanced thermoelectric performance of F4-TCNQ doped $FASnI_3$ thin films," J. Mater. Chem. A **8**, 25431–25442 (2020).
[55]H. Fischer, "Quantitative determination of heat conductivities by scanning thermal microscopy," Thermochim. Acta **425**, 69–74 (2005).
[56]G. Wielgoszewski, G. Jóźwiak, M. Babij, T. Baraniecki, R. Geer, and T. Gotszalk, "Investigation of thermal effects in through-silicon vias using scanning thermal microscopy," Micron **66**, 63–68 (2014).
[57]Y. Ge, Y. Zhang, J. M. R. Weaver, and P. S. Dobson, "Dimension-and shape-dependent thermal transport in nano-patterned thin films investigated by scanning thermal microscopy," Nanotechnology **28**(48), 485706 (2017).
[58]Y. Li, Y. Zhang, X. Xiong, and W. Yu, "Investigation of contact thermal resistance at the probe-sample interface in scanning thermal microscopy based on the fractal network model through numerical analysis," Numer. Heat Transfer, Part A **86**, 1–14 (2023).
[59]Y. Li, N. Mehra, T. Ji, and J. Zhu, "Realizing the nanoscale quantitative thermal mapping of scanning thermal microscopy by resilient tip-surface contact resistance models," Nanoscale Horiz. **3**, 505–516 (2018).
[60]Q. Zhang, W. Zhu, J. Zhou, and Y. Deng, "Realizing the accurate measurements of thermal conductivity over a wide range by scanning thermal microscopy combined with quantitative prediction of thermal contact resistance," Small **19**, 2300968 (2023).
[61]W. Chen, Y. Feng, L. Qiu, and X. Zhang, "Scanning thermal microscopy method for thermal conductivity measurement of a single SiO_2 nanoparticle," Int. J. Heat Mass Transfer **154**, 119750 (2020).
[62]J. Spièce, C. Evangeli, A. J. Robson, A. El Sachat, L. Haenel, M. I. Alonso, M. Garriga, B. J. Robinson, M. Oehme, J. Schulze, F. Alzina, C. Sotomayor Torres, and O. V. Kolosov, "Quantifying thermal transport in buried semiconductor nanostructures via cross-sectional scanning thermal microscopy," Nanoscale **13**, 10829–10836 (2021).
[63]J. Spièce, C. Evangeli, K. Lulla, A. Robson, B. Robinson, and O. Kolosov, "Improving accuracy of nanothermal measurements via spatially distributed scanning thermal microscope probes," J. Appl. Phys. **124**, 015101 (2018).
[64]Z. Liu, Y. Feng, and L. Qiu, "Near-field radiation analysis and thermal contact radius determination in the thermal conductivity measurement based on SThM open-loop system," Appl. Phys. Lett. **120**, 113506 (2022).
[65]J. Bodzenta, A. Kaźmierczak-Bałata, M. Lorenc, and J. Juszczyk, "Analysis of possibilities of application of nanofabricated thermal probes to quantitative thermal measurements," Int. J. Thermophys. **31**, 150–162 (2010).
[66]J. Bodzenta, M. Chirtoc, and J. Juszczyk, "Reduced thermal quadrupole heat transport modeling in harmonic and transient regime scanning thermal microscopy using nanofabricated thermal probes," J. Appl. Phys. **116**, 054501 (2014).
[67]J. Bodzenta, J. Juszczyk, A. Kaźmierczak-Bałata, P. Firek, A. Fleming, and M. Chirtoc, "Quantitative thermal microscopy measurement with thermal probe driven by dc + ac current," Int. J. Thermophys. **37**, 1–17 (2016).
[68]E. N. Esfahani, F. Ma, S. Wang, Y. Ou, J. Yang, and J. Li, "Quantitative nanoscale mapping of three-phase thermal conductivities in filled skutterudites via scanning thermal microscopy," Natl. Sci. Rev. **5**, 59–69 (2018).
[69]Y. Zhang, W. Zhu, L. Han, and T. Borca-Tasciuc, "Quantitative temperature distribution measurements by non-contact scanning thermal microscopy using Wollaston probes under ambient conditions," Rev. Sci. Instrum. **91**, 014901 (2020).
[70]Q. Zhu, J. Liu, Y. Lin, S. Xie, and J. Li, "Spatially resolving heterogeneous thermal conductivity of BiCuSeO based thermoelectric nanostructures via scanning thermal microscopy," Appl. Phys. Lett. **117**, 133102 (2020).
[71]J. L. Bosse, M. Timofeeva, P. D. Tovee, B. J. Robinson, B. D. Huey, and O. V. Kolosov, "Nanothermal characterization of amorphous and crystalline phases in chalcogenide thin films with scanning thermal microscopy," J. Appl. Phys. **116**, 134904 (2014).
[72]E. Guen, D. Renahy, M. Massoud, J.-M. Bluet, P.-O. Chapuis, and S. Gomes, in *2016 22nd International Workshop on Thermal Investigations of ICs and Systems (THERMINIC)* (IEEE, 2016), pp. 110–114.
[73]D. Shan, K. Pan, Y. Liu, and J. Li, "High fidelity direct measurement of local electrocaloric effect by scanning thermal microscopy," Nano Energy **67**, 104203 (2020).
[74]C. M. Frausto-Avila, V. M. Arellano-Arreola, J. M. Yañez Limon, A. De Luna-Bugallo, S. Gomès, and P.-O. Chapuis, "Thermal boundary conductance of CVD-grown MoS_2 monolayer-on-silica substrate determined by scanning thermal microscopy," Appl. Phys. Lett. **120**, 262202 (2022).
[75]J. Martinek, M. Valtr, R. Cimrman, and P. Klapetek, "Thermal conductivity analysis of delaminated thin films by scanning thermal microscopy," Meas. Sci. Technol. **25**, 044022 (2014).
[76]P. Klapetek, J. Martinek, P. Grolich, M. Valtr, and N. J. Kaur, "Graphics cards based topography artefacts simulations in scanning thermal microscopy," Int. J. Heat Mass Transfer **108**, 841–850 (2017).
[77]K. Kim, S. Jaung, J. Chung, J. Won, O. Kwon, J. S. Lee, S. Park, and Y. K. Choi, "Quantitative scanning thermal microscopy with double scan technique," Int. Conf. Micro/Nanoscale Heat Transfer **42924**, 899–904 (2008).
[78]K. Kim, J. Chung, G. Hwang, O. Kwon, J. S. Lee, S. Park, and Y. K. Choi, in *Heat Transfer Summer Conference* (ASME, 2009), Vol. 43567, pp. 543–547.

[79]D. Choi, N. Poudel, S. B. Cronin, and L. Shi, "Effects of basal-plane thermal conductivity and interface thermal conductance on the hot spot temperature in graphene electronic devices," Appl. Phys. Lett. **110**, 073104 (2017).
[80]L. Sun, W. Wang, P. Jiang, and X. Bao, "Nanoscale thermometry under ambient conditions via scanning thermal microscopy with 3D scanning differential method," Rev. Sci. Instrum. **93**, 114902 (2022).
[81]L. Ramiandrisoa, A. Allard, Y. Joumani, B. Hay, and S. Gomés, "A dark mode in scanning thermal microscopy," Rev. Sci. Instrum. **88**, 125115 (2017).
[82]F. Menges, H. Riel, A. Stemmer, and B. Gotsmann, "Quantitative thermometry of nanoscale hot spots," Nano Lett. **12**, 596–601 (2012).
[83]J. Chung, K. Kim, G. Hwang, O. Kwon, Y. K. Choi, and J. S. Lee, in *TMNN-2011. Proceedings of the International Symposium on Thermal and Materials Nanoscience and Nanotechnology* (Begel House Inc., 2011), p. 071601.
[84]E. Jung, G. Hwang, J. Chung, O. Kwon, J. Han, Y.-T. Moon, and T.-Y. Seong, "Investigating the origin of efficiency droop by profiling the temperature across the multi-quantum well of an operating light-emitting diode," Appl. Phys. Lett. **106**, 4 (2015).
[85]G. Hwang, J. Chung, and O. Kwon, "Enabling low-noise null-point scanning thermal microscopy by the optimization of scanning thermal microscope probe through a rigorous theory of quantitative measurement," Rev. Sci. Instrum. **85**, 11 (2014).
[86]G. Hwang and O. Kwon, "Measuring the size dependence of thermal conductivity of suspended graphene disks using null-point scanning thermal microscopy," Nanoscale **8**, 5280–5290 (2016).
[87]K. Yoon, G. Hwang, J. Chung, H. g. Kim, O. Kwon, K. D. Kihm, and J. S. Lee, "Measuring the thermal conductivity of residue-free suspended graphene bridge using null point scanning thermal microscopy," Carbon **76**, 77–83 (2014).
[88]G. Hwang and O. Kwon, "Quantitative temperature profiling across nanoheater on silicon-on-insulator wafer using null-point scanning thermal microscopy," Int. J. Therm. Sci. **108**, 81–88 (2016).
[89]J. Cha, H. Shin, and O. Kwon, "Vacuum null-point scanning thermal microscopy: Simultaneous quantitative nanoscale mapping of undisturbed temperature and thermal resistance," Int. J. Therm. Sci. **172**, 107268 (2022).
[90]H. Shin, S. Liu, and O. Kwon, "Quantitative nanoscale temperature mapping across the multi-quantum well of a light-emitting diode in operation using vacuum null-point scanning thermal microscopy to evaluate local energy conversion efficiency," RSC Adv. **13**, 34230–34238 (2023).
[91]K. Kondratenko, D. Hourlier, D. Vuillaume, and S. Lenfant, "Nanoscale thermal conductivity of kapton-derived carbonaceous materials," J. Appl. Phys. **131**(6), 065102 (2022).
[92]S. Gonzalez-Casal, R. Jouclas, I. Arbouch, Y. H. Geerts, C. Van Dyck, J. Cornil, and D. Vuillaume, "Thermoelectric properties of benzothienobenzothiophene self-assembled monolayers in molecular junctions," J. Phys. Chem. Lett. **15**, 11593–11600 (2024).
[93]N. Harnack, S. Rodehutskors, and B. Gotsmann, "Scanning thermal microscopy method for self-heating in nonlinear devices and application to filamentary resistive random-access memory," ACS Nano **19**, 5342–5352 (2025).
[94]D. G. Cahill and R. O. Pohl, "Thermal conductivity of amorphous solids above the plateau," Phys. Rev. B **35**, 4067 (1987).
[95]S. Lefèvre and S. Volz, "3ω-scanning thermal microscope," Rev. Sci. Instrum. **76**(3), 033701 (2005).
[96]M. Chirtoc, J. Gibkes, R. Wernhardt, J. Pelzl, and A. Wieck, "Temperature-dependent quantitative 3ω scanning thermal microscopy: Local thermal conductivity changes in NiTi microstructures induced by martensite-austenite phase transition," Rev. Sci. Instrum. **79**(9), 093703 (2008).
[97]V. Leitgeb, K. Fladischer, L. Mitterhuber, and S. Defregger, in *2019 25th International Workshop on Thermal Investigations of ICs and Systems (THERMINIC)* (IEEE, 2019), pp. 1–4.
[98]D. Trefon-Radziejewska, J. Juszczyk, M. Krzywiecki, G. Hamaoui, N. Horny, J.-S. Antoniow, and M. Chirtoc, "Thermal characterization of morphologically diverse copper phthalocyanine thin layers by scanning thermal microscopy," Ultramicroscopy **233**, 113435 (2022).
[99]A. Altes, R. Heiderhoff, and L. J. Balk, "Quantitative dynamic near-field microscopy of thermal conductivity," J. Phys. D: Appl. Phys. **37**, 952–963 (2004).
[100]G. Pernot, A. Metjari, H. Chaynes, M. Weber, M. Isaiev, and D. Lacroix, "Frequency domain analysis of 3ω-scanning thermal microscope probe application to tip/surface thermal interface measurements in vacuum environment," J. Appl. Phys. **129**, 055105 (2021).
[101]Z. Liu, Y. Feng, H. Li, N. Cao, and L. Qiu, "Quantitative analysis of interface heat transport at the Si_3N_4/SiO_2 van-der waals point contact," Int. J. Heat Mass Transfer **232**, 125979 (2024).
[102]T. Borca-Tasciuc, A. R. Kumar, and G. Chen, "Data reduction in 3ω method for thin-film thermal conductivity determination," Rev. Sci. Instrum. **72**, 2139–2147 (2001).
[103]L. Shi, D. Li, C. Yu, W. Jang, D. Kim, Z. Yao, and P. Kim, "A Majumdar measuring thermal and thermoelectric properties of one-dimensional nanostructures using a microfabricated device," J. Heat Transfer **125**, 881–888 (2003).
[104]P. Janus, D. Szmigiel, A. Sierakowski, M. Rudek, and T. Gotszalk, "Active calibration reference of minimized height for characterization of scanning thermal microscopy systems," Ultramicroscopy **221**, 113188 (2021).
[105]A. Reihani, Y. Luan, S. Yan, J. W. Lim, E. Meyhofer, and P. Reddy, "Quantitative mapping of unmodulated temperature fields with nanometer resolution," ACS Nano **16**, 939–950 (2022).
[106]T. P. Nguyen, L. Thiery, S. Euphrasie, E. Lemaire, S. Khan, D. Briand, L. Aigouy, S. Gomes, and P. Vairac, "Calibration tools for scanning thermal microscopy probes used in temperature measurement mode," J. Heat Transfer **141**, 071601 (2019).
[107]A. Dawson, M. Rides, A. S. Maxwell, A. Cuenat, and A. R. Samano, "Scanning thermal microscopy techniques for polymeric thin films using temperature contrast mode to measure thermal diffusivity and a novel approach in conductivity contrast mode to the mapping of thermally conductive particles," Polym. Test. **41**, 198–208 (2015).
[108]W. J. Parker, R. J. Jenkins, C. P. Butler, and G. L. Abbott, "Flash method of determining thermal diffusivity," J. Appl. Phys. **32**, 1679–1684 (1961).
[109]Z. Umatova, Y. Zhang, R. Rajkumar, P. S. Dobson, and J. M. R. Weaver, "Quantification of atomic force microscopy tip and sample thermal contact," Rev. Sci. Instrum. **90**, 095003 (2019).
[110]M. Chirtoc, J. Bodzenta, and A. Kaźmierczak-Bałata, "Calibration of conductance channels and heat flux sharing in scanning thermal microscopy combining resistive thermal probes and pyroelectric sensors," Int. J. Heat Mass Transfer **156**, 119860 (2020).
[111]T. P. Nguyen, E. Lemaire, S. Euphrasie, L. Thiery, D. Teyssieux, D. Briand, and P. Vairac, "Microfabricated high temperature sensing platform dedicated to scanning thermal microscopy (SThM)," Sens. Actuators, A **275**, 109–118 (2018).
[112]Y. Ge, Y. Zhang, J. A. Booth, J. M. R. Weaver, and P. S. Dobson, "Quantification of probe–sample interactions of a scanning thermal microscope using a nanofabricated calibration sample having programmable size," Nanotechnology **27**, 325503 (2016).
[113]B. Pruchnik, P. Smagowski, D. Badura, T. Piasecki, W. Połacik, P. Putek, and T. Gotszalk, "Transformer bridge-based metrological unit for scanning thermal microscopy with resistive nanoprobes," Meas. Sci. Technol. **35**, 085901 (2024).
[114]M. E. McConney, D. D. Kulkarni, H. Jiang, T. J. Bunning, and V. V. Tsukruk, "A New twist on scanning thermal microscopy," Nano Lett. **12**, 1218–1223 (2012).
[115]P. Janus, A. Sierakowski, P. Grabiec, M. Rudek, W. Majstrzyk, and T. Gotszalk, "Micromachined active test structure for scanning thermal microscopy probes characterization," Microelectron. Eng. **174**, 70–73 (2017).
[116]B. Yang, M. Lenczner, S. Cogan, F. Menges, H. Riel, B. Gotsmann, P. Janus, and G. Boetch, in *2014 15th International Conference on Thermal, Mechanical and Mulit-Physics Simulation and Experiments in Microelectronics and Microsystems (EuroSimE)* (IEEE, 2014), pp. 1–6.

[117]K. Hwang, K. Kim, J. Chung, O. Kwon, B. Lee, J. S. Lee, S. Park and Y. K. Choi, in *International Conference on Micro/Nanoscale Heat Transfer* (ASME, 2009), Vol. 43901, pp. 421–425.
[118]H. Chae, G. Hwang, and O. Kwon, "Fabrication of scanning thermal microscope probe with ultra-thin oxide tip and demonstration of its enhanced performance," Ultramicroscopy **171**, 195–203 (2016).
[119]P. Janus, A. Sierakowski, M. Rudek, P. Kunicki, A. Dzierka, P. Biczysko, and T. Gotszalk, "Thermal nanometrology using piezoresistive SThM probes with metallic tips," Ultramicroscopy **193**, 104–110 (2018).
[120]J. Hirotani, J. Amano, T. Ikuta, T. Nishiyama, and K. Takahashi, "Carbon nanotube thermal probe for quantitative temperature sensing," Sens. Actuators, A **199**, 1–8 (2013).
[121]M. Timofeeva, A. Bolshakov, P. D. Tovee, D. A. Zeze, V. G. Dubrovskii, and O. V. Kolosov, "Scanning thermal microscopy with heat conductive nanowire probes," Ultramicroscopy **162**, 42–51 (2016).
[122]K. Nam, H. Kim, J. Im, J. S. Ahn, and S. Choi, "Enhancing optical contrast of sub-wavelength optical image using graphene oxide coated probe in scanning thermal microscopy," Appl. Phys. Lett. **122**, 213505 (2023).